DIELECTRIC RELAXATION AND ELECTROOPTICAL EFFECTS IN NEMATIC LIQUID CRYSTALS

A dissertation submitted
to Kent State University in partial
fulfillment of the requirements for the
Degree of Doctor of Philosophy

By

Ye Yin

December 2007

Dissertation written by

Ye Yin

B.S., Beijing Normal University, 2001

Ph.D., Kent State University, 2007

Approved by

__Oleg D. Lavrentovich_____, Chair, Doctoral Dissertation Committee

__Sergij V. Shiyanovskii_____, Members, Doctoral Dissertation Committee

__Philip J. Bos_____

__Deng-ke Yang_____

__Samuel Sprunt_____

Accepted by

__Oleg D. Lavrentovich_____, Chair, Chemical Physics Interdisciplinary Program

__John R. D. Stalvey_____, Dean, College of Arts and Sciences

TABLE OF CONTENTS

LIST OF FIGURES

LIST OF TABLES

ACKNOWLEDGEMENTS

I am greatly thankful to my advisor, Dr. Oleg D. Lavrentovich, for his continuous guidance and support to me throughout my graduate student career. His knowledge and enthusiasm in science always inspired me and had been a strong motivation for me to exploit new knowledge. His valuable suggestions and persistent help are my most valuable asset during these years. Without him, I would not be able to finish this work.

I am greatly thankful to my co-advisor, Dr. Sergij. V. Shiyanovskii. His profound knowledge of physics can always catch the essence of some superficial phenomena and extract the most valuable question behind. His foresightedness in physics always helps me to find the shortcut to solve the complicated problem.

I also wish to express my special gratitude to Dr Peter Palffy-Muhoray, Dr Deng-ke Yang, Dr. Phil. Bos and Dr. Sameul Sprunt, for the guidance and advice during the time I spend in their labs. I would like to thank Dr. L.-C. Chen, Dr Antal Jakli, Dr. David Allender, Dr. Eugene Gartland and all CPIP faculty members who passed on precious knowledge to me. I would like to thank the committee members to participate for my defense and share their valuable comments.

My final and most heartfelt thank goes to my wife, Xinyuan Li, and my parents for their support, encouragement, companionship, and understanding throughout my graduate study here.

Chapter 1

INTRODUCTION

Liquid crystals (LCs) represent a special state of soft matter in which the anisotropic molecules or their aggregates demonstrate a long-range orientational order but little or no positional long-range order [1]. In the simplest case of a uniaxial nematic LC (NLC), the long-range positional order is absent altogether; the molecules form a uniaxial centrosymmetric medium, as they are predominantly aligned along a single direction called a director and described by a unit vector $\mathbf{n}$ (such that $\mathbf{n} \equiv -\mathbf{n}$). The director can be realigned by electric and magnetic fields that thus change the optical properties of sample. The orientational dynamics of director in the applied electric field is a fundamental physical phenomenon that is at the heart of modern display technologies. Discovered in 1930s by Frederiks (initially for the magnetic case) [2], this phenomenon, rather surprisingly, still poses a fundamental unanswered question regarding the behavior of NLCs with the finite rate of dielectric relaxation. The problem can be understood as follows.

The dielectric torque that reorients the director has the density $\mathbf{M}(t) = \mathbf{D}(t) \times \mathbf{E}(t)$, where $\mathbf{E}(t)$ is the electric field and $\mathbf{D}(t)$ is the electric displacement at the moment of

time t. In the widely accepted standard approach [1, 3, 4], the electric response is assumed to be *instantaneous*, i.e., the displacement $\mathbf{D}(t)$ is determined by the electric field at *the very same moment* $\mathbf{D}(t) = \varepsilon_0 \boldsymbol{\varepsilon} \mathbf{E}(t)$, where $\varepsilon_0 = 8.8542 \times 10^{-12}$ C^2 N^{-1} m^{-2} is the free space permittivity, $\boldsymbol{\varepsilon}$ is the relative permittivity tensor. Such an approximation is certainly valid when the director reorientation time in NLC is much longer than the time of dielectric relaxation. However, it might be not valid when the driving field is switched quickly. The dielectric relaxation is determined by a number of processes, some of which (electronic polarizability, intra-molecular vibrations) are very fast, with a characteristic time less than a nanosecond, while others, such as reorientation of the permanent molecular dipoles are slow, with the typical relaxation time τ of the order of 0.01-1 ms [5, 6]. If the external field changes over the time comparable to τ, then it is intuitively clear that the dielectric response should depend not only on the present value of the electric field, but also on its past values. This effect is well known for isotropic fluids and solid crystals, see for example, the classic book by Fröhlich [7], but not for the NLCs. The effect of dielectric relaxation in NLCs is intrinsically more complex than in isotropic fluids and solid crystals, because the dielectric tensor changes with the applied field (as the result of director reorientation).

The objective of this thesis is to explore the effect of dielectric relaxation on NLC director reorientation and reveal the physics of time-dependent dielectric response of NLCs. The knowledge of the time-dependent dielectric response of NLCs can be directly used to investigate how to realize the fast switching of NLCs. From the application point

of view, to speed up the NLC switching driven by electric field is important for display industry. Nematic cells can be switched very quickly, for example, within 0.1 ms for a cell of a thickness 10-15 μm [8], or even faster, as demonstrated by N. Clark's group [9]. From the standard model, the NLC switching time $\tau \propto \left(\Delta\varepsilon U^2\right)^{-1}$ is inversely proportional to the voltage square U^2 and the dielectric anisotropy $\Delta\varepsilon$ [3, 8]. Consequently, increasing the voltage U is an effective way to shorten the NLC response time. However, the experiments with high applied voltages exhibit some delays in response, that cannot be explained by the standard model [9]. In this thesis, we propose a general model to describe the time-dependent dielectric response of NLC. We found that the non-removable delay is actually the effect of dielectric relaxation on NLC dynamics. We also found that this dielectric relaxation effect also influences the dielectric heating of NLCs. Unlike those heating effects found in isotropic dielectrics, the dielectric heating in NLC behaves in a more complicated way. For some particular NLCs with special dielectric properties, such as the reversible sign of $\Delta\varepsilon$ during the dielectric relaxation frequency range, we found there is a new bistability called thermodielectric bistability which is caused by the anisotropic nature of NLC dielectric heating and director reorientation in an electric field. We present experiments to support the model and explore quantitatively the relation among the NLC dielectric anisotropy, the dielectric memory effect during switching, and the thermodielectric bistability.

The contents of this thesis are covered by the publications listed below.

- "Fast switching optical modulator based on Dual Frequency Nematic Cell", Y.

Yin, M. Gu, A. B. Golovin, S. V. Shiyanovskii, O. D. Lavrentovich; Mol. Cryst. Liq. Cryst. **421**, 133 (2004).

- "Dielectric torque and orientation dynamics of liquid crystals with dispersion", Y. Yin, S. V. Shiyanovskii, A. B. Golovin, O. D. Lavrentovich; Phys. Rev. Lett. **95**, 087801 (2005).
- "Electric Heating Effects in Nematic Liquid Crystals", Y. Yin, S. V Shiyanovskii, O. D. Lavrentovich; J. Appl. Phys., **100**, 024906 (2006).
- "Electric Heating Induced Liquid Crystal Bistability", Y. Yin, S. V Shiyanovskii, O. D. Lavrentovich; Phys. Rev. Lett, **98**, 097801 (2007).
- "Fast Switching of Nematic Liquid Crystals in an Electric Field: Effects of Dielectric Relaxation on the Director and Thermal Dynamics", in Chapter 10 of *Thermotropic Liquid Crystals, Recent Advance*, A. Ramamoorthy (Editor), London, Springer (2007). ISBN 1402053274.

1.1 Organization of the dissertation

In Chapter 1, the background knowledge related to the time-dependent dielectric response of NLCs will be briefly introduced. Section 1.2 covers the fundamental theory of the NLC dynamics driven by the electric field. In section 1.3, we give an overview of the NLC electro-optics. In section 1.4, we review how the dielectric relaxation occurs in

NLCs in the assumption that the electric field causes no director reorientation. In section 1.4, we discuss the origins of the electromagnetic field induced heating effect of NLCs.

In Chapter 2, we investigate the effect of dielectric relaxation on NLC director reorientation dynamics. In section 2.1, we propose a general model to quantitatively describe the director orientation dynamics in which the dielectric permittivity tensor is no longer constant during the switching process. The proposed model expresses the electric displacement $\mathbf{D}(t)$ (as well as the dielectric torque density $\mathbf{M}(t)$) as the function of the static dielectric properties of the NLC, the present and past electric field and director. In section 2.2, we present experimental data characterizing the frequency and temperature dependent dielectric permittivities of a dual-frequency nematic (DFN). We use DFN to carry out an electrical switching experiment in which the standard ‘‘instantaneous’’ model and our model predict effects of opposite signs. The experimental data support the latter model.

In Chapter 3, we explore a closely related problem of dielectric heating that is most pronounced in the region of dielectric relaxation. We build a model to explain the fact that the NLC temperature increase is determined by multiple factors, such as the electric field **E**, the dielectric anisotropy and its frequency dependency of NLC, and the thermal properties of the surrounding medium.

In Chapter 4, we report on the novel bistability effect caused by the anisotropic nature of dielectric heating and director reorientation in the electric field. The effect is called a thermodielectric bistability. Unlike the conventional LC bistabilities caused by

the balance of the surface anchoring and electric field, the thermodielectric bistability is induced by the electric field alone, through its dual coupling with the liquid crystal, namely, the dielectric reorientation and dielectric heating.

Chapter 5 concludes the thesis with a summary of research and outlook for the future investigations.

1.2 Basics of Nematodynamics

The specific set of problems for deformation and flow of the nematic systems under stress and external (magnetic and electrical) fields is described by the term nematodynamics. The complete set of the equations to describe the nematodynamics include [1, 4]

(1) the continuity equation corresponding to mass conservation:

$$\partial\rho/\partial t = -\nabla\cdot\rho\mathbf{v}\,, \qquad (1.1)$$

(2) Navier-Stocks equation describing the conserved components of the linear momentum:

$$\frac{\partial\rho v_i}{\partial t} = -\frac{\partial}{\partial x_j}\left(-\sigma_{ij} + \rho v_i v_j\right), \qquad (1.2)$$

(3) torque equation describing the director dynamics:

$$I\frac{d}{dt}\left[\mathbf{n}\times\dot{\mathbf{n}}\right] = \left[\mathbf{n}\times\mathbf{h}\right] + \mathbf{\Gamma} + \mathbf{M}\,, \qquad (1.3)$$

where ρ is the fluid density, $\mathbf{v}$ is the fluid velocity, σ_{ij} is the elastic Eriksen stress tensor, I is the moment of inertial per unit volume. The molecular field $\mathbf{h}$ is

$$\mathbf{h} = K_{11}\nabla(\nabla\cdot\mathbf{n}) - K_{22}[\mathbf{A}_1\nabla\times\mathbf{n} + \nabla\times(\mathbf{A}_1\mathbf{n})] + K_{33}[\mathbf{A}_2\times\nabla\times\mathbf{n} + \nabla\times(\mathbf{n}\times\mathbf{A}_2)], \qquad (1.4)$$

where K_{11}, K_{22} and K_{33} are the elastic constant for splay, twist and bend deformations of the NLC, respectively. For one-constant approximation, when the elastic constants of the LC are taken equal to each other ($K = K_{11} = K_{22} = K_{33}$), $\mathbf{h}$ can be simplified as $\mathbf{h} = K\nabla^2\mathbf{n}$. $\mathbf{\Gamma}$ is the viscous torque,

$$\mathbf{\Gamma} = (\alpha_2 - \alpha_3)[\mathbf{n}\times\mathbf{N}] + (\alpha_5 - \alpha_6)[\mathbf{n}\times\mathbf{A}\cdot\mathbf{n}], \qquad (1.5)$$

here α_k ($k \in [1,6]$) are Leslie viscosity coefficients, $\mathbf{N} = \dot{\mathbf{n}} - \varpi\times\mathbf{n}$ is the relative director rotation rate, $\mathbf{A}$ is the strain-rate tensor. The first term on the right hand side (RHS) of (1.5) is induced by the rotational viscosity, and the second term is induced by the back-flow effect, $\mathbf{M}(t) = \mathbf{D}(t)\times\mathbf{E}(t)$ is the dielectric torque at the moment t.

The standard way to calculate $\mathbf{M}$ is based on representing the electric displacement $\mathbf{D}(t)$ as a function of the electric field at the very same moment t [1],

$$\mathbf{D}(t) = \varepsilon_0\varepsilon_\perp\mathbf{E}(t) + \varepsilon_0(\varepsilon_\parallel - \varepsilon_\perp)\big(\mathbf{n}(t)\cdot\mathbf{E}(t)\big)\mathbf{n}(t), \qquad (1.6)$$

where $\varepsilon_\parallel$ and $\varepsilon_\perp$ are the parallel ($\mathbf{E}\parallel\mathbf{n}$) and perpendicular ($\mathbf{E}\perp\mathbf{n}$) dielectric permittivity, respectively, $\Delta\varepsilon = \varepsilon_\parallel - \varepsilon_\perp$ is called the dielectric anisotropy. Therefore the electric torque reads

$$\mathbf{M}(t) = \varepsilon_0(\varepsilon_\parallel - \varepsilon_\perp)\mathbf{n}(t)\times\mathbf{E}(t)\cdot\big[\mathbf{n}(t)\cdot\mathbf{E}(t)\big]. \qquad (1.7)$$

Equation (1.7) of the standard model assumes that the dielectric response of NLC is instantaneous, which is not always true. In this dissertation, we propose a model to describe the electric torque $\mathbf{M}$ by taking into account that the electric displacement $\mathbf{D}(t)$ depends not only on the instantaneous values of the applied electric field and the director, but also on the "prehistory" of these values.

Although the above equations provide the approach to deal with the most general case of the nematodynamics, under certain simplified situation we do not need all of them, (1.1) - (1.5), to study the NLC system based on some widely-used assumptions. The assumptions include: (a) the NLC bulk is regarded as an incompressible unit, i.e., $\partial\rho/\partial t = 0$; (b) if there is no external angular momentum, the internal angular momentum $I\frac{d}{dt}[\mathbf{n}\times\dot{\mathbf{n}}]$ equals to zero; (c) the velocity gradient of the NLC layer is so tiny that the backflow term in (1.5), $(\alpha_5-\alpha_6)[\mathbf{n}\times\mathbf{A}\cdot\mathbf{n}]$, is negligibly small compared with the rotational viscosity term, $(\alpha_2-\alpha_3)[\mathbf{n}\times\mathbf{N}]$. With the assumptions (a) to (c) and one-elastic-constant assumption, the director dynamics equation can be simplified as:

$$\left[\mathbf{n}\times K\nabla^2\mathbf{n}\right]+(\alpha_2-\alpha_3)[\mathbf{n}\times\mathbf{N}]+\mathbf{M}=0\,. \qquad (1.8)$$

The above assumptions are valid for the NLC system of this dissertation because our NLC system is one thin NLC layer (~10 μm) which is confined in between two parallel electrodes and exposed to the electric field. The NLC layer can be regarded as an incompressible unit, and has no external angular momentum. In addition, we employ a simplified hydrodynamic approach neglecting the backflow effects. This approach is

justified, as we shall see from chapter 2, where the difference between the experiment and standard model is most evident, corresponds to a small phase change of about 1 rad, and thus to a relatively small reorientation of **n** , by about 3^{o}.

We will analyze the limitation of the standard model and derive the general expression of $\mathbf{M}(t)$ in Chapter 2.

1.3 Electro-optics of NLC

The electro-optical application of NLCs has made a huge success in the display industry. We will use a simple NLC system to give an overview of the principle of electro-optics of NLC.

Let us restrict the discussion on the in-plane rotation of **n** with zero hydrodynamic flow with the valid assumptions (a) to (c) mentioned in section 1.2, the torque equation (1.3) can then be simplified to the following scalar form,

$$K\frac{\partial^2\theta}{\partial z^2}+\varepsilon_0\Delta\varepsilon E^2\sin\theta\cos\theta=\gamma_1\frac{\partial\theta}{\partial t}, \qquad (1.9)$$

where θ is the angle between the director **n** and the cell normal, $\gamma_1=\alpha_2-\alpha_3$ is the rotational viscosity. Equation (1.9) specifies that the sign of $\Delta\varepsilon$ determines the direction of the rotation of NLCs. For NLC with $\Delta\varepsilon>0$, **n** reorients parallel to **E**; if $\Delta\varepsilon<0$, then $\mathbf{n}\perp\mathbf{E}$. If the NLC is confined between two parallel electrodes separated by a distance d, the boundary condition for θ is then determined by $\theta(z=0)$ and $\theta(z=d)$.

The coordinate and field dependent director reorientation angle $\theta(z,t)$ are found numerically using (1.9) supplemented with the boundary conditions.

We turn now to the discussion how the linear polarized light propagates in the nematic medium. We consider the simplest case with a plane monochromatic incident beam. The incident optical wave splits into two waves, ordinary wave (o-wave) and extraordinary wave (e-wave). For the o-wave, the NLC behaves as an isotropic medium with the refraction index $n_o = \sqrt{\varepsilon_\perp}$. The e-wave has the refraction index n_{eff} that depends on the angle β between **n** and the wave vector **k** [3, 4],

$$n_{eff} = \frac{n_o n_e}{\sqrt{n_e^2 \cos^2\beta + n_o^2 \sin^2\beta}}, \qquad (1.10)$$

where $n_e = \sqrt{\varepsilon_\parallel}$ is the extraordinary refraction index, $\Delta n = n_e - n_o$ is the optical birefringence.

The optical birefringence of NLCs and the possibility to orient the director by an applied electric field leads to many practical applications. One standard setup to realize the electric controlled birefringence includes the light source, two crossed polarizers and the cell of two parallel electrodes filled with NLC, where the NLC cell is placed between two crossed polarizers.

The optical retardance ΔL between e-wave and o-wave for light of wavelength λ traveled a distance d within the liquid crystal layer can be represented by [3, 4],

$$\Delta L = \int_0^d \left[n_{eff}(z) - n_o \right] dz \,. \qquad (1.11)$$

The intensity of light passing through the cell depends on the angle φ_0 between the polarization vector of the incident beam and the initial orientation of **n** [3, 4],

$$I = I_0 \sin^2 2\varphi_0 \sin^2(\pi\Delta L/\lambda), \qquad (1.12)$$

where I_0 is the intensity of the incident beam.

Electrically-controlled LC cells are at the heart of many modern optical applications, such as LC displays, optical retarders, beam deflectors, polarization rotators, etc [3]. In many cases (for example, in LC optical phased arrays [10] and adaptive optics [11]), a desirable mode of operation is to switch a large phase retardation, say, one wavelength, within a short period of time, say, one millisecond. According to (1.11), the maximum optical retardance $\Delta L_{\max} = (n_e - n_o)d$ is a linear function of the cell thickness d, while the switching time varies as d^2 [3]. When the field is switched off, a typical LC cell with $n_e - n_o \approx 0.2$ and $d \approx 5\,\mu\text{m}$ switches $\Delta L_{\max} \approx 1\,\mu\text{m}$ within $\tau_{off} = \gamma d^2/\pi^2 K \sim 25$ ms, where $\gamma \sim 0.1\,\text{kgm}^{-1}\text{s}^{-1}$ and $K \sim 10^{-11}\,\text{N}$ are the characteristic rotation viscosity and elastic constant of the LC, respectively [3]. The figure of merit $FoM = \Delta L_{\max}^2/\pi^2\tau_{off}$, expressed in terms of the material parameters $FoM = K(n_e - n_o)^2/\gamma$ is typically (1-10) $\mu\text{m}^2\text{s}^{-1}$ [12]. To resolve the contradictory requirements of a short response time and large amplitude of switched optical retardations, several approaches have been explored:

(a), Recent synthesis advances produced nematic materials with $FoM \sim 10^2$ $\mu\text{m}^2\text{s}^{-1}$, but only at elevated temperatures $80^0 - 100^0\text{C}$ [13].

(b), Passing the beam through the cell many times increases FoM, as ΔL increases while $\tau_{off} = const$; multiple passes, however, increase light losses .

(c), Employing dual frequency nematic (DFN) cells, in which the director relaxation towards its stable planar state parallel to the bounding plates is assisted by high frequency voltage pulses [11]; the scheme switches $L = 0.13\,\mu m$ within 0.8 ms, i.e., $FoM = \Delta L_{\max}^2 / \pi^2 \tau_{off} \approx 2\,\mu m^2 s^{-1}$.

Compared with (a) and (b), the advantage of method (c) has less light loss and possibility to operate at room temperature (although the physical parameters of DFN are temperature sensitive). The DFNs used in (c) are specially designed NLCs in which the low frequency (<100 KHz) dielectric relaxation of parallel permittivity $\varepsilon_{\parallel}$ and the constant $\varepsilon_{\perp}$ up to MHz leads to a strong frequency dependent $\Delta\varepsilon$ with sign reversal property. The empirical description of dielectric relaxation will be discussed in the following section.

1.4 Dielectric relaxation of NLC

When a dielectric is influenced by an external electric field, it reaches a new equilibrium state though a new process called the dielectric relaxation [14]. The dielectric relaxation is a reflection of the fact that the electric displacement $\mathbf{D}(t)$ needs a finite time to adjust to the value of the electric field $\mathbf{E}(t)$.

The superposition rule in the classical electromagnetic theory results in the following dependence of $\mathbf{D}(t)$ on the past and present values of the electric field $\mathbf{E}(t)$ [15]:

$$\mathbf{D}(t) = \varepsilon_0 \mathbf{E}(t) + \mathbf{P}(t) = \varepsilon_0 \mathbf{E}(t) + \varepsilon_0 \int_{-\infty}^{t} \mathbf{P}(t,t')dt' = \varepsilon_0 \mathbf{E}(t) + \varepsilon_0 \int_{-\infty}^{t} \boldsymbol{\alpha}(t,t')\mathbf{E}(t')dt', \qquad (1.13)$$

where $\mathbf{P}(t,t') = \varepsilon_0 \boldsymbol{\alpha}(t,t')\mathbf{E}(t')$ is the polarization describing the contribution of the past electric field $\mathbf{E}(t')$ on the current $\mathbf{D}(t)$. The electric polarization $\mathbf{P}(t)$ is the vector field that expresses the density of permanent or induced electric dipole moments in a dielectric material. The step response function $\boldsymbol{\alpha}(t,t')$ is also called a decay function, because it vanishes when $t - t' \to \infty$. If the dielectric properties of the medium do not change with time, e.g. solid crystals, then $\boldsymbol{\alpha}(t,t')$ is a function of the time interval $\bar{t} = t - t'$ only,

$$\boldsymbol{\alpha}(t,t') = \boldsymbol{\alpha}(\bar{t}) = \boldsymbol{\alpha}(t - t'). \qquad (1.14)$$

If (1.14) holds, then the harmonic electric field $\mathbf{E}(t) = \mathbf{E}_\omega e^{-i\omega t}$ produces the harmonic electric displacement $\mathbf{D}(t)$ with the same angular frequency ω,

$$\mathbf{D}(t) = \varepsilon_0 \left(\mathbf{I} + \int_0^\infty \boldsymbol{\alpha}(\bar{t}) e^{i\omega \bar{t}} d\bar{t} \right) \mathbf{E}_\omega e^{-i\omega t} = \mathbf{D}_\omega e^{-i\omega t}. \qquad (1.15)$$

where $\mathbf{D}_\omega$ is

$$\mathbf{D}_\omega = \varepsilon_0 \boldsymbol{\varepsilon}(\omega) \mathbf{E}_\omega, \qquad (1.16)$$

and the frequency dependent dielectric permittivity $\boldsymbol{\varepsilon}(\omega)$ is

$$\boldsymbol{\varepsilon}(\omega) = \mathbf{I} + \int_0^\infty \boldsymbol{\alpha}(\bar{t}) e^{i\omega \bar{t}} d\bar{t}, \qquad (1.17)$$

where $\mathbf{I}$ is a unit tensor.

Equation (1.16), the well-known dielectric response equation in the frequency domain, is equivalent to (1.13) if the assumption (1.14) holds. However, in LC, when

the director reorients ($\mathbf{n}(t') \neq const$), the dielectric tensor varies with the director orientation. Therefore, equation (1.14) is not true if the orientational dynamics of the NLC is considered. In chapter 2, we will explore how the dielectric relaxation affects the NLC orientational dynamics.

Before we explore the dielectric dispersion effects, it is important to understand the basics of a dielectric relaxation in NLCs.

There are three different mechanisms contributing to the electric polarization $\mathbf{P}(t)$ in (1.13) and thus to $\mathbf{D}(t)$: (1) electronic polarization, (2) molecular polarization, and (3) orientational polarization.

Electronic polarization comes from the electric field induced displacement of electron cloud. Molecular polarization is caused by the relative displacement of the atomic groups within the molecule. Orientational polarization is caused by the influence of orientational order on molecular motion.

Different from the electronic and molecular polarizations, orientational polarization only exists in polar materials, i.e., those with molecules having a permanent dipole moment. Orientational polarization depends on the extent to which the applied field can order the permanent dipoles against the disordering effect of the thermal energy of their environment. All of these polarization mechanisms can only operate up to a limiting frequency, after which a further frequency increase will result in their disappearance. Because of the oscillator-like nature of the forces involved, this is accompanied by an absorption of the resonance type for electronic and atomic polarization, but for

orientational polarization the disappearance, accompanied by a broader peak in the loss factor, is more gradual, because the mechanism involved is of the relaxation type, and may involve a broad distribution of relaxation times.

These three mechanisms have very different characteristic relaxation times [5, 16-18]. One can use Planck's equation to estimate ω of electronic and molecular motions, and then obtain the magnitude order of the polarization times for electronic and molecular polarizations. The Planck's equation reads $\tilde{E} = hf = \frac{h\omega}{2\pi}$, where $h = 6.626 \times 10^{-34}\ \mathrm{J \cdot s}$ is the Planck's constant, $\tilde{E}$ is the energy of the particle of interest, electron (for electronic polarization) or molecule (molecular polarization). For electronic polarization, $\tilde{E} \approx 1\mathrm{eV} = 1.602 \times 10^{-19}\ \mathrm{J}$, one can get the characteristic electronic polarization time $\tau_E = h / 2\pi\tilde{E} \approx 10^{-16}\ \mathrm{s}$. For molecular polarization, $\tilde{E} \approx 10^{-4}\ \mathrm{eV}$, one can get the characteristic molecular polarization time $\tau_M = h / 2\pi\tilde{E} \approx 10^{-12}\ \mathrm{s}$. To investigate in the range near the characteristic polarization time, say [$10^{-1}\tau$, $10^{1}\tau$], one need consider the corresponding polarization effect.

The orientational polarization of NLCs, associated with the reorientation of permanent molecular electric dipoles, is relatively slow with the time scales ranging from 10^{-9} s to 10^{-2} s, which covers the NLC reorientation characteristic times [10^{-4}, 10^{-2}] s [3]. On the other hand, electronic and molecular polarizations are needed to be considered in a much shorter time scale compared with NLC reorientation; therefore, in the rest part of this section, we will focus on the discussion of the dielectric behavior of NLC related to the orientational polarization.

Consider such a NLC molecule with the longitudinal $\mathbf{p}_l$ and transversal $\mathbf{p}_t$ permanent dipole moments in an isotropic phase. There are two relaxation modes: mode 1, rotations of $\mathbf{p}_t$ around the long axis, and mode 2, reorientation of $\mathbf{p}_l$, Figure 1.

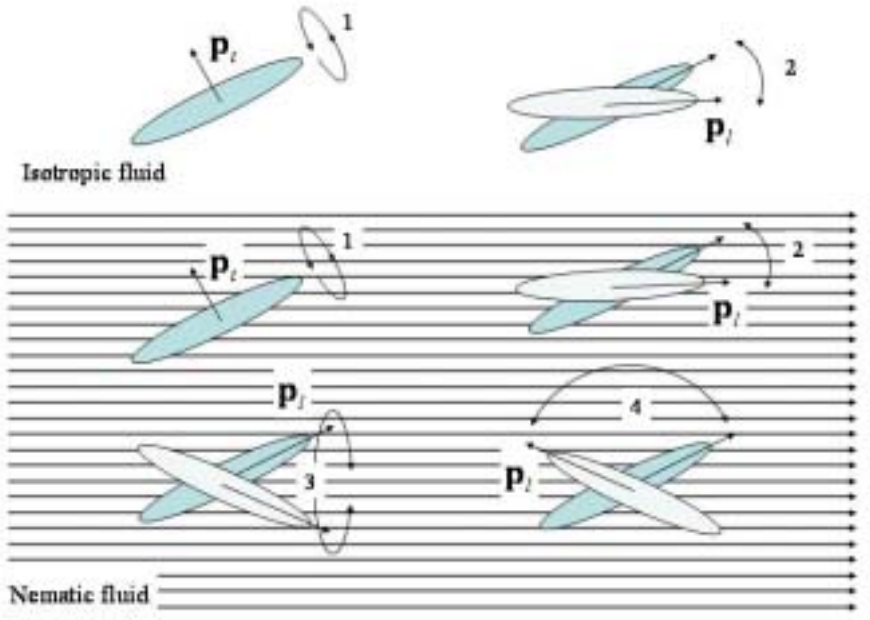

Figure 1. Orientational relaxation modes for a molecule in an isotropic fluid (top) and in a nematic medium (bottom).

The mode 1 has a smaller relaxation time, $\tau_1 < \tau_2$, because of the smaller moments of inertia involved. When this isotropic fluid is cooled down into the NLC phase, the dynamics is affected by the appearance of the "nematic" potential associated with the orientational order along the director $\mathbf{n}$. The mode 1 remains almost the same as in the isotropic phase, and contributes to perpendicular component of dielectric polarization (determined with respect to $\mathbf{n}$). Mode 2 is associated with small changes of the angle

between $\mathbf{p}_l$ and $\mathbf{n}$; it contributes to the parallel component of dielectric polarization. Mode 3 is associated with conical rotations of $\mathbf{p}_l$ around the director (as the axis of the cone); it is effective when the applied electric field is perpendicular to $\mathbf{n}$ and contributes to the perpendicular component of the dielectric polarization. Finally, mode 4 is a qualitatively different mode related with the flip-flops of $\mathbf{p}_l$. The molecular reorientations in mode 4 are hindered by the nematic surrounding of the molecule as in the middle point of the flip-flop it finds itself perpendicular to $\mathbf{n}$. The relaxation time for the mode 4 is thus significantly larger than the relaxation time of any other mode. Typically, $\tau_1 < \tau_2, \tau_3 < \tau_4$; τ_4 might be as large as few milliseconds in some NLCs [19].

With more than one relaxation mechanism involved, the step response tensor function is represented as a superposition,

$$\boldsymbol{\alpha}(t,t') = \sum_k \boldsymbol{\alpha}_k(t,t'), \qquad (1.18)$$

where $\boldsymbol{\alpha}_k(t,t')$ is the step response tensor function of a certain relaxation mode. To obtain the explicit dependencies, one should know the step response function which is generally dependent on the relaxation type. Based on different definition of $\boldsymbol{\alpha}_k(t,t')$, a number of the relaxation models have been developed [5, 14, 16-18, 20-24]. Among all the models, Debye model is developed earliest and used most widely [20]. Debye model assumes $\alpha(t,t')$ decays exponentially with the relaxation time constant τ,

$$\alpha(\bar{t}) = \bar{\alpha}\exp\left(-\frac{\bar{t}}{\tau}\right), \qquad (1.19)$$

where $\bar{\alpha}$ is the coefficient to be determined later. The hypothesis (1.19), combined with the definition of $\varepsilon(\omega)$,

$$\varepsilon(\omega) = 1 + \int_0^\infty \alpha(\bar{t}) e^{i\omega\bar{t}} d\bar{t} \qquad (1.20)$$

predicts how the dielectric permittivity should depend on the frequency of the applied harmonic field:

$$\varepsilon(\omega) = 1 + \frac{\bar{\alpha}\tau}{1 - i\omega\tau}. \qquad (1.21)$$

Equation (1.21) tells us that the real part of the dielectric permittivity decreases from the "static" value $\varepsilon_s = 1 + \bar{\alpha}\tau$ at low frequencies to a high frequency value $\varepsilon_f = 1$ at $\omega \to \infty$. In reality, ε_f is different from 1 because of the electronic and intra-molecular processes at high frequencies. Therefore, $\alpha(t,t')$ in Debye model can be represented by,

$$\alpha(t,t') = \frac{\varepsilon_s - \varepsilon_f}{\tau} \exp\left(-\frac{t-t'}{\tau}\right), \qquad (1.22)$$

where ε_s is the slow dielectric constant. Inserting (1.22) into (1.17), one can obtain

$$\varepsilon^*(\omega) = \varepsilon_f + \frac{\varepsilon_s - \varepsilon_f}{1 - i\omega\tau}. \qquad (1.23)$$

The real part of $\varepsilon^*(\omega)$ is

$$\varepsilon^r(\omega) = \varepsilon_f + \frac{\varepsilon_s - \varepsilon_f}{1 + \omega^2\tau^2}, \qquad (1.24)$$

and the imaginary part of $\varepsilon^*(\omega)$ is

$$\varepsilon^i(\omega) = \omega\tau \frac{\varepsilon_s - \varepsilon_f}{1 + \omega^2\tau^2}. \qquad (1.25)$$

The relation between $\varepsilon^i(\omega)$ and $\varepsilon^r(\omega)$ can be easily obtained via (1.24) and (1.25),

$$\left(\varepsilon^i(\omega)\right)^2 = \left(\varepsilon_s - \varepsilon^r(\omega)\right)\left(\varepsilon^r(\omega) - \varepsilon_f\right). \qquad (1.26)$$

Figure 2(a) shows $\varepsilon^r(\omega)$ and $\varepsilon^i(\omega)$ of the standard Debye dielectric relaxation as a function of $\omega\tau$ are shown in Figure 2(a). An alternative way to present $\varepsilon^r(\omega)$ and $\varepsilon^i(\omega)$ is shown in Figure 2(b), in which we plot $\varepsilon^i(\omega)$ vs $\varepsilon^r(\omega)$. Equation (1.26) implies that the points ($\varepsilon^r(\omega)$, $\varepsilon^i(\omega)$) lie on a semicircle.

ε_s and ε_f correspond to the left and the right end of the semicircle. The way to represent $\varepsilon^i(\omega)$ as a function of $\varepsilon^r(\omega)$ in the Debye relaxation is also called a Cole-Cole plot [25].

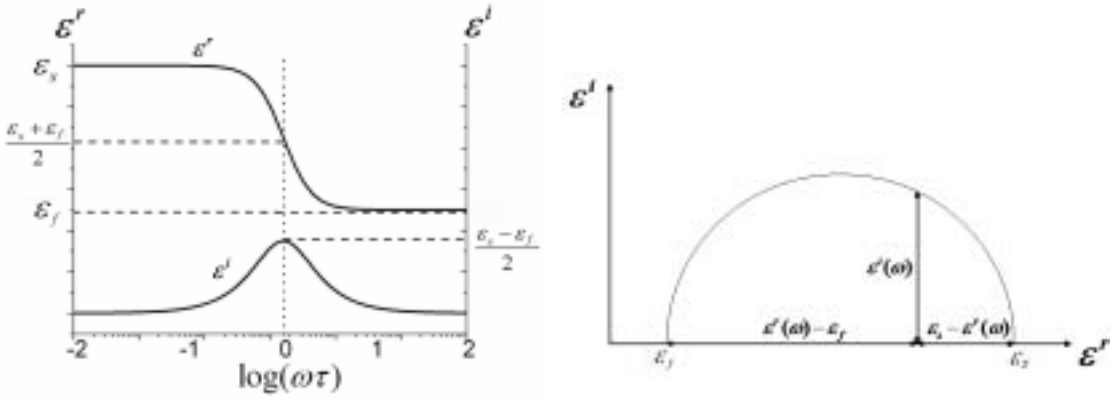

(a) (b)

Figure 2. $\varepsilon^r(\omega)$ and $\varepsilon^i(\omega)$ of the standard Debye dielectric relaxation. (a) $\varepsilon^r(\omega)$ and $\varepsilon^i(\omega)$ as a function of $\omega\tau$; (b) ε^i as a function of ε^r, $\varepsilon^i(\varepsilon^r)$.

Although Debye equation (1.23)-(1.26) describes the dielectric relaxation of a large number of condensed systems, serious deviations might happen for many other systems, such as mixtures, polymers and some disordered solids. Several extensions of Debye model have been developed, such as Cole-Cole relaxation mode [26, 27], Cole-Davidson mode [28, 29] with $a = 0$ and $b \in (0,1)$, and Havriliak-Negami mode [30]. The general form of all these modes can be represented as,

$$\varepsilon^*(\omega) = \varepsilon_f + \frac{\varepsilon_s - \varepsilon_f}{\left(1 - (i\omega\tau)^{1-a}\right)^b}. \qquad (1.27)$$

where $a \in [0,1]$ and $b \in [0,1]$. For the Cole-Cole relaxation mode, $a \in (0,1)$ and $b = 1$; for the Cole-Davidson mode, $a = 0$ and $b \in (0,1)$; for the Havriliak-Negami mode, $a \in (0,1)$ and $b \in (0,1)$. The dependencies $\varepsilon^r(\omega)$ and $\varepsilon^i(\omega)$ of the non-Debye relaxation are demonstrated in Figure 3.

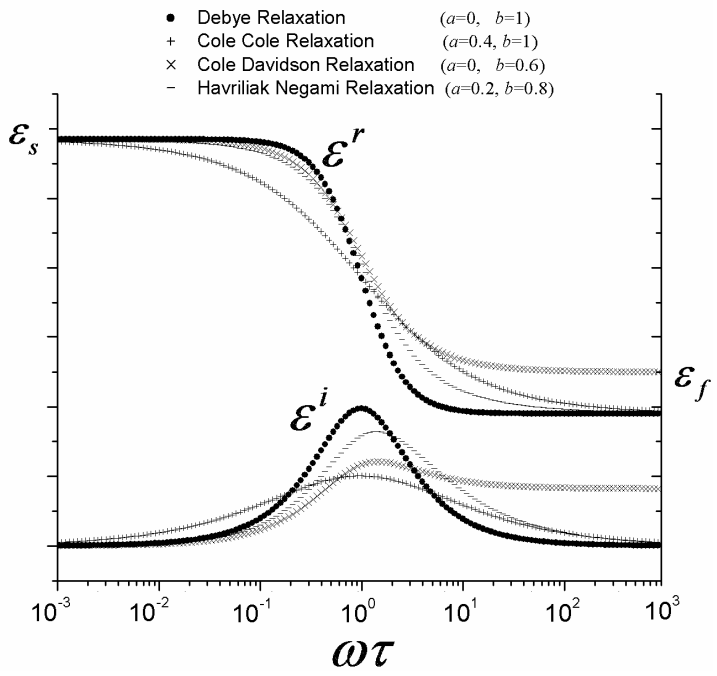

Figure 3. $\varepsilon^r(\omega)$ and $\varepsilon^i(\omega)$ of the Debye and Non-Debye dielectric relaxation.

Let us now apply this Debye model to the orientational relaxation modes of a nematic with fixed director, $\mathbf{n}(t') = const$, assuming that each $\boldsymbol{\alpha}_k$ in (1.18) follows the Debye behavior (1.19). Using (1.17) and (1.18), we find

$$\boldsymbol{\varepsilon}(\omega) = \boldsymbol{\varepsilon}_h + \sum_{k=1}^{4} \frac{\Delta\boldsymbol{\varepsilon}_k}{1+\omega\tau_k}. \qquad (1.28)$$

where $\Delta\boldsymbol{\varepsilon}_k = \bar{\boldsymbol{\alpha}}_k \tau_k$ is the maximum contribution by the kth mode to the real part of the dielectric tensor, the summation is taken over the orientational modes 1-4 only and $\boldsymbol{\varepsilon}_h$ is generally different from the unit tensor, as discussed above.

By choosing an appropriate mutual orientation of the probing electric field $\mathbf{E}$ and the director $\mathbf{n}$, one can measure the dielectric relaxation spectra for the parallel geometry, $\varepsilon_{\parallel}$,

$\mathbf{E} \| \mathbf{n}$, or for the perpendicular geometry, $\varepsilon_{\perp}$, $\mathbf{E} \perp \mathbf{n}$. The relaxation modes 1, 2 and 4 contribute to the component $\varepsilon_{\|}$, and modes 1 and 3 contribute to $\varepsilon_{\perp}$. Figure 4 illustrates a typical frequency dependence of the dielectric components for a nematic material with all the relaxation modes (1-4) taken into account.

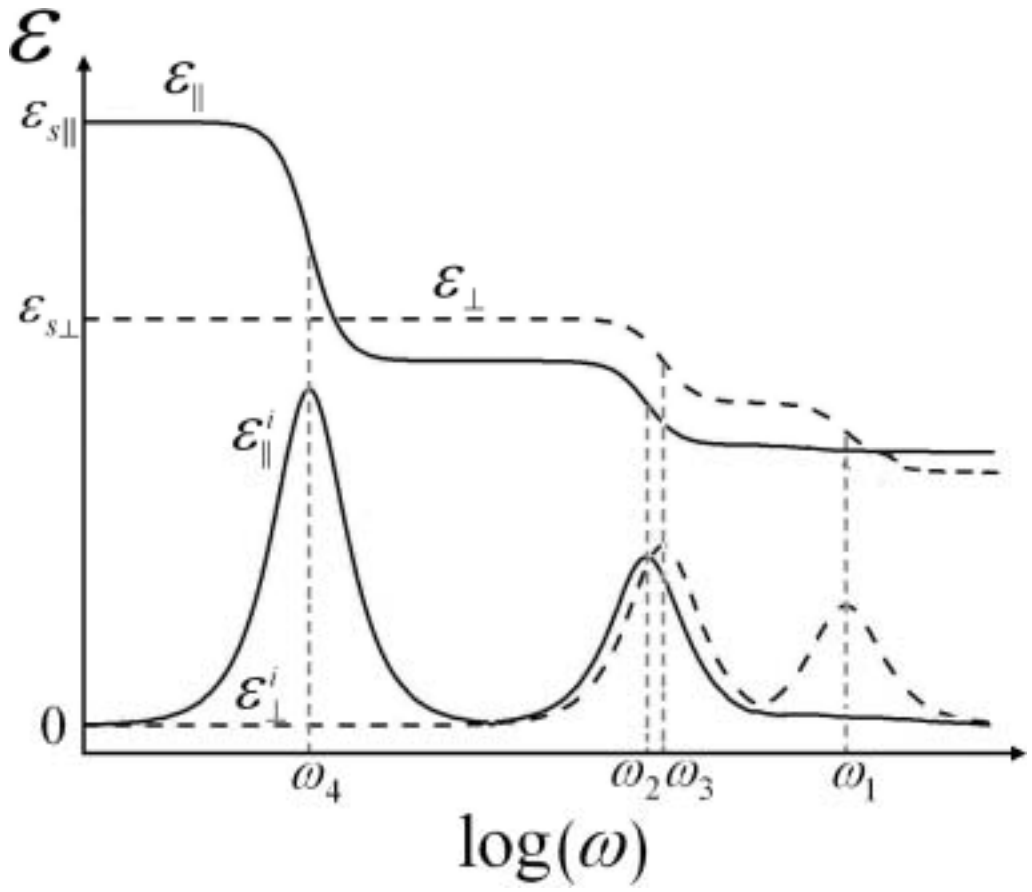

Figure 4. A typical frequency dependence of real and imaginary parts of the components of the dielectric permittivity tensor for a nematic material.

From Figure 4, we know there are multiple longitudinal and transversal relaxation times due to different relaxation mode. In most situations, the slowest relaxation mode is

concerned only since other relaxation processes are too fast to interact with the director reorientation. In the rest of the dissertation, $\tau_{\parallel}$ will be used to represent the largest relaxation time of $\varepsilon_{\parallel}$, i.e., $\tau_{\parallel} = \tau_4$; $\tau_{\perp}$ will be used to represent the largest relaxation time of $\varepsilon_{\perp}$ i.e., $\tau_{\perp} = \tau_3$. Many research efforts have been put to relate the values of $\tau_{\parallel}$ and $\tau_{\perp}$ to molecular parameters [31-36].

Meier and Saupe found that the longitudinal relaxation time $\tau_{\parallel}$ is related to the potential barrier parameter η [31-33],

$$\eta = q / RT , \qquad (1.29)$$

where q is the barrier height of the flip-flops around the short axis, R is the gas constant, and T is the temperature. Through the introduction of η, Meier and Saupe derived the following formula [31-33],

$$\frac{\tau_{\parallel}}{\tau_0} = \frac{\exp\eta - 1}{\eta}, \qquad (1.30)$$

where τ_0 corresponds to a hypothetical state with $q = 0$. τ_0 is approximately equal to the relaxation time of the nematics in the isotropic phase τ_{is}.

A much smaller barrier exists when the molecules rotate around the director **n** than other axes. Additionally, the nematic order facilitates this type of motions, so that the ratio of the transverse relaxation time $\tau_{\perp}$ and τ_0 is even less than one [34-36],

$$\frac{\tau_{\perp}}{\tau_0} < 1 . \qquad (1.31)$$

From (1.30) and (1.31), the ratio $\tau_{\parallel}/\tau_{\perp}$ can be estimated by an established potential barrier parameter η. Normally, $\tau_{\parallel}/\tau_{\perp} \sim [1,10^3]$ in NLC [37, 38]. The values of $\tau_{\parallel}$ and $\tau_{\perp}$ of some typical NLCs are shown in Table 1. $\tau_{\perp}$ is typically in the nanosecond ranges, so that the transverse relaxation process is usually regarded as a fast process compared with the NLC director dynamics. However, for certain NLCs, $\tau_{\parallel}$ may be as large as microsecond, which is comparable to some fast director orientational dynamics [39].

Table 1. $\tau_{\parallel}$ and $\tau_{\perp}$ of certain typical NLCs.

Material	$\tau_{\parallel}$ (ns)	$\tau_{\perp}$ (ns)	T (K)	Reference
5CB	40	24	307	[40]
6CB	31.8	5.3	301	[41]
7CB	33	2.2	306	[42]
8CB	53	4	303	[43]
MLC2048	5134	64	305	[8, 44]

A particularly interesting case occurs when the static value of $\varepsilon_{\parallel}$ exceeds that of $\varepsilon_{\perp}$. In this case, as a result of the low-frequency dispersion (mode 4) in $\varepsilon_{\parallel}$, there is a possibility that $\varepsilon_{\parallel}$ will turn out to be smaller than $\varepsilon_{\perp}$ in the relaxation frequency region. Consequently, the dielectric anisotropy changes its sign from positive to negative at a certain cross-over frequency f_c. The NLC with the property to change the sign of dielectric anisotropy is called a dual frequency nematic (DFN). Strictly speaking, most typical NLCs with positive anisotropy can be regarded as DFN with a very high cross-over frequency; for example, the mostly widely used NLC, pentylcyanobiphenyl (5CB) is

DFN with f_c=15 MHz [45]. The sign reversal of dielectric anisotropy allows one to drive the NLC in both ways, $\mathbf{n} \| \mathbf{E}$ and $\mathbf{n} \perp \mathbf{E}$, by simply change the frequency applied voltage. The characteristics of DFN will be further discussed in Chapter 2.

1.5 Dielectric heating of NLC

Dielectric heating is caused by the absorption of electromagnetic energy in the dielectric medium through reorientation of the molecular dipoles and the associated molecular friction. The heating mechanism in isotropic dielectrics is well known, and the major application of the dielectric heating, namely, the microwave heating, is used for food processing. The food exposed to the microwave at the frequency 2.5 GHz is heated effectively since f=2.5 GHz is the relaxation frequency of water. Dielectric heating effects in the nematic liquid crystals (NLCs) are less useful since the induced temperature changes cause the change of the liquid crystal properties and thus affect the NLC switching behavior.

The first model of dielectric heating in NLC has been developed by M. Schadt [46]. In his model, the temperature decrease across the bounding (glass) plates of the NLC cell was considered negligibly small. The corresponding experiment on dielectric heating was performed for NLC cells of thickness 15 μm by placing a 80 μm thermocouple at one of the silver electrodes (apparently outside the cell). These studies were expanded in our previous work by using a much smaller thermocouple inserted directly into the NLC

slab [44]. Recently, Wu et al. proposed a new, noncontact, method [47] based on the measurements of phase retardation changes caused by the temperature-induced changes of the birefringence Δn of the NLC. This technique is applicable when the electric field causes no reorientation of the director (otherwise the phase retardation would change because of the director reorientation), i.e. when the following conditions are satisfied: (1) the material has a negative dielectric anisotropy, $\Delta\varepsilon(f)<0$, (2) the cell yields a strict planar alignment (zero pretilt angle) and (3) the electric field causes no hydrodynamics. Because of these limitations, the technique cannot address some general issue of dielectric heating in the region of dielectric relaxation for $\varepsilon_{\parallel}(f)$. The dielectric heating is especially efficient when the frequency of the applied field is close to the frequency region of dielectric relaxation, as described below.

We start from the energy conservation law [15, 48],

$$-\nabla\cdot\mathbf{S}=\frac{\partial W}{\partial t}+P_d\,, \qquad (1.32)$$

where the Poynting vector $\mathbf{S}=\mathbf{E}\times\mathbf{H}$ (W m^{-2}) determines the power flux [15, 48], W (J m^{-3}) is the electromagnetic energy density, P_d is the power dissipation density. Equation (1.32) implies the power flow equals to the difference of the power storage and the power dissipation. Therefore, the electromagnetic power density dissipation can be described by the divergence of Poynting vector [15],

$$\begin{aligned}-\nabla\cdot\mathbf{S}&=\mathbf{E}\cdot(\nabla\times\mathbf{H})-\mathbf{H}\cdot(\nabla\times\mathbf{E}) \qquad (1.33)\\ &=\mathbf{E}\cdot\frac{\partial\mathbf{D}}{\partial t}+\mathbf{H}\cdot\frac{\partial\mathbf{B}}{\partial t}+\mathbf{E}\cdot\mathbf{J}_u\end{aligned}\,,$$

where the current density $\mathbf{J}_u$ is the product of the electrical conductivity σ and the electric field, i.e., $\mathbf{J}_u = \sigma\mathbf{E}$. The harmonic electric field $\mathbf{E}$ is

$$\mathbf{E} = \frac{1}{2}\left(\mathbf{E}_\omega e^{-i\omega t} + \mathbf{E}_\omega^* e^{i\omega t}\right) = \mathbf{E}_0 \cos\left(\omega t - \varphi_0\right), \qquad (1.34)$$

and $\frac{\partial \mathbf{D}}{\partial t}$ is

$$\frac{\partial \mathbf{D}}{\partial t} = \frac{i\varepsilon_0\omega}{2}\left(-\boldsymbol{\varepsilon}(\omega)\mathbf{E}_\omega e^{-i\omega t} + \boldsymbol{\varepsilon}^*(\omega)\mathbf{E}_\omega^* e^{i\omega t}\right), \qquad (1.35)$$

where the star sign * designates the complex conjugate, $\mathbf{E}_0$ is the electric field amplitude, φ_0 is the initial phase of the applied field. Similar analysis is used to obtain the time dependent magnetic field $\mathbf{H}$ and $\frac{\partial \mathbf{B}}{\partial t}$. Therefore, equation (1.33) is rewritten as

$$\begin{aligned} -\nabla\cdot\mathbf{S} = {} & \frac{i\omega\varepsilon_0}{4}\left(\mathbf{E}_\omega\boldsymbol{\varepsilon}^*(\omega)\mathbf{E}_\omega^* - \mathbf{E}_\omega^*\boldsymbol{\varepsilon}(\omega)\mathbf{E}_\omega + \mathbf{E}_\omega^*\boldsymbol{\varepsilon}^*(\omega)\mathbf{E}_\omega^* e^{2i\omega t} - \mathbf{E}_\omega\boldsymbol{\varepsilon}(\omega)\mathbf{E}_\omega e^{-2i\omega t}\right) \\ & + \frac{i\omega\mu_0}{4}\left(\mathbf{H}_\omega\boldsymbol{\mu}^*(\omega)\mathbf{H}_\omega^* - \mathbf{H}_\omega^*\boldsymbol{\mu}(\omega)\mathbf{H}_\omega + \mathbf{H}_\omega^*\boldsymbol{\mu}^*(\omega)\mathbf{H}_\omega^* e^{2i\omega t} - \mathbf{H}_\omega\boldsymbol{\mu}(\omega)\mathbf{H}_\omega e^{-2i\omega t}\right). \\ & + \frac{\sigma}{4}\left(\mathbf{E}_\omega\mathbf{E}_\omega^* + \mathbf{E}_\omega^*\mathbf{E}_\omega + \mathbf{E}_\omega^*\mathbf{E}_\omega^* e^{2i\omega t} + \mathbf{E}_\omega\mathbf{E}_\omega e^{-2i\omega t}\right) \end{aligned} \qquad (1.36)$$

For $\mathbf{E}$ with a typical kilohertz frequency, the period of $\mathbf{E}$ is at millisecond level. For optical field, the period is at the order of 10^{-14} s. The cycle of the electromagnetic field is usually less than millisecond (<10^{-3} s), which is far smaller than the characteristic time (~ 10^0 s) of the absorption. In another word, the storage of electromagnetic power is small enough to ignore, i.e., $\left\langle \frac{\partial W}{\partial t} \right\rangle = 0$. Therefore, it is helpful to make use of the time average of (1.36) to obtain the time averaged electromagnetic heating power density P_d,

$$P_d = \left\langle -\nabla\cdot\mathbf{S} \right\rangle = \frac{\omega\varepsilon_0\mathbf{E}_0\cdot\boldsymbol{\varepsilon}^i(\omega)\cdot\mathbf{E}_0}{2} + \frac{\omega\mu_0\mathbf{H}_0\cdot\boldsymbol{\mu}^i(\omega)\cdot\mathbf{H}_0}{2} + \sigma\mathbf{E}_0\cdot\mathbf{E}_0, \qquad (1.37)$$

where the angular brackets denote the time average. The three terms on the right hand side of (1.37) correspond to the three sources of the electromagnetic heating: the dielectric heating, the induction heating, and the Ohmic heating.

Dielectric heating occurs when the electric dipoles do not align instantaneously with the electric field. The power density of the dielectric heating is $\frac{\omega\varepsilon_0\mathbf{E}_0\cdot\boldsymbol{\varepsilon}^i(\omega)\cdot\mathbf{E}_0}{2}$. A non zero $\boldsymbol{\varepsilon}^i(\omega)$ means the phase of $\mathbf{D}(t)$ lags that of the excitation $\mathbf{E}(t)$, which leads to a dissipation of power within the dielectric system. Induction heating occurs when the magnetic dipoles do not align instantaneously with the magnetic field. The power density of induction heating is $\frac{\omega\mu_0\mathbf{H}_0\cdot\boldsymbol{\mu}^i(\omega)\cdot\mathbf{H}_0}{2}$. A non zero $\boldsymbol{\mu}^i(\omega)$ means the phase of the magnetic induction $\mathbf{B}(t)$ lags that of the excitation of the magnetic field $\mathbf{H}(t)$, which leads to a dissipation of the power within the diamagnetic system. Ohmic heating is associated with the movement of the free charges, the power density of Ohmic heating is $\sigma\mathbf{E}_0\cdot\mathbf{E}_0$. When the external electric field is applied to the NLC cell, the electric heating comprises of two heating modes, dielectric heating and Ohmic heating.

The electric heating power density is related to the applied electric field frequency ω, the magnitude of the electric field $\mathbf{E}$ and the imaginary permittivity $\boldsymbol{\varepsilon}^i(\omega)$. Consequently, the electric heating causes the NLC temperature change and affects the performance of the LC devices.

Suppose the electric field with the strength 1 V/μm and frequency 100 kHz is applied to a 10-μm thick cell placed in the still air with heat transfer coefficient $k \sim 10$ W m^{-2} K^{-1},

the magnitude of imaginary permittivity $\varepsilon^i(\omega)$ is about 1, and the conductivity σ is about 10^{-8} $\Omega^{-1}m^{-1}$, one can find the total electric heating power density $P_d \approx (\omega\varepsilon_0\varepsilon^i/2+\sigma)E^2$ is at the order of 2×10^6 W/m^3 and the NLC temperature increase can be as large as 10 ^{0}C.

In summary, the dielectric heating becomes non negligible during the electric field induced NLC orientational dynamics especially when the field frequency is close to the relaxation frequency of liquid crystals [46].

Chapter 2

MEMORY EFFECT OF NEMATIC LIQUID CRYSTAL SWITCHING

In this chapter, we demonstrate that the finite rate of dielectric relaxation in NLCs which has been ignored previously causes profound effects in the fast dielectric reorientation of the director. We propose a theory of dielectric response in which the electric displacement depends not only on the present (as in the standard theory) but also on the past values of electric field and director. We design an experiment with DFN in which the standard ‘‘instantaneous’’ model and our model predict effects of opposite signs; the experimental data support the latter model.

2.1 Theory

From Chapter 1, we know that due to the dielectric relaxation processes the electric displacement $\mathbf{D}(t)$ is dependent not only on the current electric field $\mathbf{E}(t)$ but also the past electric field $\mathbf{E}(t'<t)$, (1.13). The well-known dielectric response equation ($\mathbf{D}_\omega = \varepsilon_0 \boldsymbol{\varepsilon}(\omega)\mathbf{E}_\omega$) is equivalent to equation (1.13) if the assumption $\boldsymbol{\alpha}(t,t') = \boldsymbol{\alpha}(t-t')$, holds. However, $\boldsymbol{\alpha}(t,t') = \boldsymbol{\alpha}(t-t')$ is not true if the orientational dynamics of the NLC is considered, when $\mathbf{n}(t') \neq const$. Below we will derive the relation between $\boldsymbol{\alpha}(t,t')$ and

$\boldsymbol{\alpha}(t-t')$ for fixed director and explore how the dielectric relaxation affects the NLC orientational dynamics.

As we discussed in (1.18), the dielectric step response tensor function $\boldsymbol{\alpha}(t,t')$ of NLCs is a sum of contributions of many relaxation modes, $\boldsymbol{\alpha}(t,t') = \sum_k \boldsymbol{\alpha}_k(t,t')$, where $\boldsymbol{\alpha}_k(t,t')$ is the step response tensor function of a certain relaxation mode.

If a certain relaxation process is sufficiently fast, so that both the electric field and the director can be considered constant during the relaxation period, then,

$$\int_{-\infty}^{t} \boldsymbol{\alpha}_k(t,t')\mathbf{E}(t')dt' = \mathbf{E}(t)\int_{-\infty}^{t} \boldsymbol{\alpha}_k(t-t')dt'. \qquad (2.1)$$

We can now attribute each $\boldsymbol{\alpha}_k(t,t')$ to the "fast" $\boldsymbol{\alpha}_f(t,t')$ and the "slow" $\boldsymbol{\alpha}_s(t,t')$ term based on the condition (2.1) that depends on the rates with which the electric field and director change, so that $\boldsymbol{\alpha}(t,t') = \boldsymbol{\alpha}_f(t,t') + \boldsymbol{\alpha}_s(t,t')$ and the electric displacement $\mathbf{D}(t)$ of the NLC can be written as

$$\mathbf{D}(t) = \varepsilon_0 \boldsymbol{\varepsilon}_f(t)\mathbf{E}(t) + \varepsilon_0 \int_{-\infty}^{t} \boldsymbol{\alpha}_s(t,t')\mathbf{E}(t')dt'. \qquad (2.2)$$

where the fast term $\boldsymbol{\varepsilon}_f(t)$ is:

$$\boldsymbol{\varepsilon}_f(t) = \mathbf{I} + \int_{-\infty}^{t} \boldsymbol{\alpha}_f(t,t')dt'. \qquad (2.3)$$

The fast term $\boldsymbol{\varepsilon}_f(t)$ has the stationary diagonal form in the current local frame associated with the director, thus its time dependence originates from reorientation of the local frame and is determined in a uniaxial NLC only by the current director orientation $\mathbf{n}(t)$:

$$\boldsymbol{\varepsilon}_f(t) = \varepsilon_{f\perp}\mathbf{I} + \left(\varepsilon_{f\parallel} - \varepsilon_{f\perp}\right)\mathbf{n}(t) \otimes \mathbf{n}(t). \qquad (2.4)$$

where $\varepsilon_{f\parallel}$ and $\varepsilon_{f\perp}$ are the components of the tensor in the diagonal form, and $\otimes$ stands for the external product of two vectors, which is the tensor with the components $\left[\mathbf{n}(t)\otimes\mathbf{n}(t)\right]_{ij} = n_i(t)n_j(t)$. If the all relaxation processes are sufficiently fast to satisfy the condition (2.1), then the integral term in (2.2) disappears and we get the standard description:

$$\mathbf{D}(t) = \varepsilon_0 \boldsymbol{\varepsilon}(t)\mathbf{E}(t)\,. \qquad (2.5)$$

To derive relation between $\boldsymbol{\alpha}_s(t,t')$ and $\boldsymbol{\alpha}_s(t-t')$ we have to investigate how rotation of the local frame affects slow relaxation processes. As one can see in section 1.4, only the relaxation processes associated with the reorientation of molecules with permanent electric dipoles may violate condition (2.1) and be attributed as slow. The reorientation occurs in the potential profile caused by the intermolecular interactions. The potential profile in a uniaxial NLC has axial symmetry with two potential valleys for a long molecular axis parallel and antiparallel to the to the director $\mathbf{n}$. The relaxation processes correspond to reorientation within a valley or to transition from between valleys. The latter is significantly slower because the molecules rotate through unfavorable orientations and need to overcome the associated potential barrier of the intermolecular interactions. The potential barriers should keep the polarization orientation fixed with respect to the director $\mathbf{n}$, and thus when $\mathbf{n}$ reorients, it should drag the polarization. We assume that this director-mediated rotation does not affect the reorientation relaxation of the individual molecules. This assumption seems reasonable even when the rotation speed of $\mathbf{n}$ is comparable with the relaxation rate of polarization,

because the slow rotation of all molecules with $\mathbf{n}$ should not affect substantially the fast reorientation of small portion of molecules that are responsible for the dielectric relaxation.

In uniaxial NLC, we can analyze the director reorientation effect on slow contribution $\mathbf{P}_s(t,t')$ in current polarization separately for parallel $\mathbf{P}_s^{\parallel}(t,t')$ and perpendicular $\mathbf{P}_s^{\perp}(t,t')$ components with respect to the current director $\mathbf{n}(t)$. $\mathbf{P}_s^{\parallel}(t,t')$ is simply dragged by the director being always parallel to $\mathbf{n}(t)$. The component $\mathbf{P}_1^{\perp}(t,t')$ of $\mathbf{P}_s^{\perp}(t,t')$ that is perpendicular to $\dot{\mathbf{n}}(t)$ and $\mathbf{n}(t)$ remains unaffected whereas the component $\mathbf{P}_2^{\perp}(t,t')$ of $\mathbf{P}_s^{\perp}(t,t')$ that lies in the plane of $\dot{\mathbf{n}}(t)$ and $\mathbf{n}(t)$ rotates to be perpendicular to $\mathbf{n}(t)$, see Figure 5. Therefore, we can introduce the local frame $\{\mathbf{n}(t),\mathbf{l}(t),\mathbf{m}(t)\}$ with arbitrary initial orientation of $\mathbf{l}(t_0)$ and $\mathbf{m}(t_0)$ at the moment t_0, when the electric field is applied. This frame rotates with angular velocity $\boldsymbol{\Omega}(t)=-\dot{\mathbf{n}}(t)\times\mathbf{n}(t)$, so that:

$$\dot{\mathbf{v}}(t)=\boldsymbol{\Omega}(t)\times\mathbf{v}(t)=-\left[\dot{\mathbf{n}}(t)\times\mathbf{n}(t)\right]\times\mathbf{v}(t), \qquad (2.6)$$

where $\mathbf{v}(t)=\mathbf{n}(t),\mathbf{l}(t),\mathbf{m}(t)$; (2.6) becomes identity for $\mathbf{v}(t)=\mathbf{n}(t)$. The dielectric relaxation in this frame does depend on the director rotation and thus $\boldsymbol{\alpha}_s(t,t')$ in the laboratory frame can be expressed through the step response function tensor components $\alpha_{s\parallel}(t-t')$ and $\alpha_{s\perp}(t-t')$ parallel and perpendicular to the director, when the director is fixed:

$$\boldsymbol{\alpha}_s(t,t')=\alpha_{s\parallel}(t-t')\mathbf{n}(t)\otimes\mathbf{n}(t')+\alpha_{s\perp}(t-t')\left[\mathbf{l}(t)\otimes\mathbf{l}(t')+\mathbf{m}(t)\otimes\mathbf{m}(t')\right]. \qquad (2.7)$$

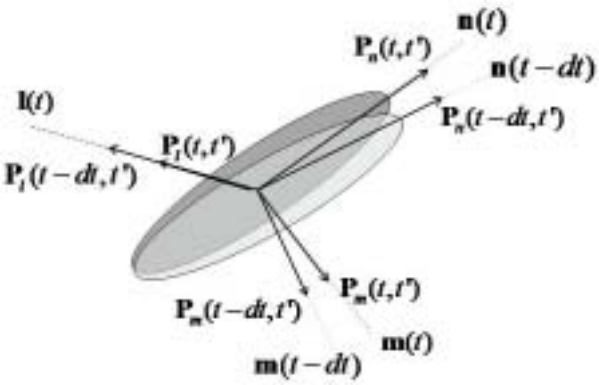

Figure 5. The demonstration of the transient rotation of the uniaxial NLC during $[t-dt,t]$.

In the case of biaxial NLC, we assume that the potential barriers around all three directors ($\mathbf{l},\mathbf{m},\mathbf{n}$) keep the corresponding polarization components parallel to these directors, (2.8), and that this director rotations do not affect the relaxation and $\boldsymbol{\alpha}_s(t,t')$ in the local frame, Figure 6. Therefore, $\boldsymbol{\alpha}_s(t,t')$ in the laboratory frame can be expressed through the step response function tensor component $\alpha_\nu(t-t')$ along the director, when the director is fixed:

$$\boldsymbol{\alpha}_s(t,t') = \sum_\nu \alpha_\nu(t-t')\mathbf{v}(t)\otimes\mathbf{v}(t'), \qquad (2.8)$$

and the electric displacement $\mathbf{D}(t)$ of the biaxial NLC can then be written as

$$\mathbf{D}(t) = \varepsilon_0\boldsymbol{\varepsilon}_f(t)\mathbf{E}(t) + \varepsilon_0\sum_{\mathbf{v}}\int_{-\infty}^{t}\alpha_\nu(t-t')\mathbf{v}(t)\otimes\mathbf{v}(t')\mathbf{E}(t')dt'. \qquad (2.9)$$

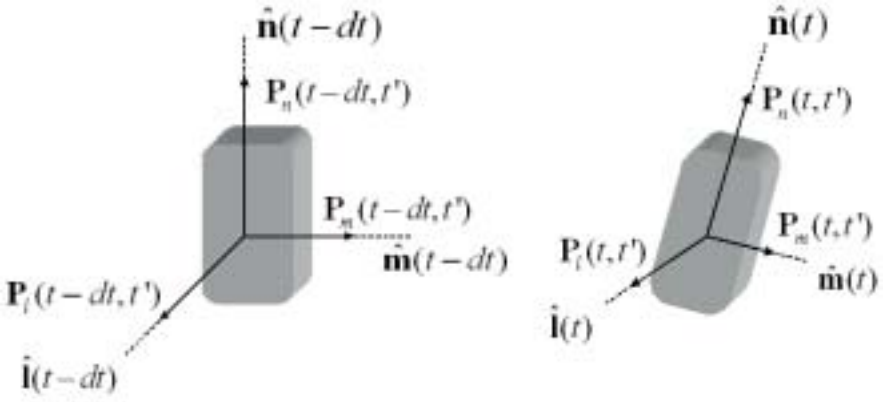

Figure 6. The schematic demonstration of the transient rotation of the biaxial NLC during $[t-dt,t]$.

The step response functions $\alpha_\nu(t-t')$ for the uniaxial and the biaxial NLC, can be reconstructed from the frequency dispersion of the dielectric tensor. However, it is more practical to assume certain dependence and then verify it experimentally. The classical Debye's theory of relaxation predicts the exponential decay of $\alpha_\nu(t-t')$ and Lorenzian behavior for $\alpha_\nu(\omega)$ [7, 14, 20]:

$$\alpha_\nu(t-t') = \frac{\varepsilon_{l\nu}-\varepsilon_{h\nu}}{\tau_\nu}\exp\left(-\frac{t-t'}{\tau_\nu}\right), \qquad (2.10)$$

$$\alpha_\nu(\omega) = \frac{\varepsilon_{l\nu}-\varepsilon_{h\nu}}{1-\omega\tau_\nu}, \qquad (2.11)$$

where $\varepsilon_{l\nu}$ and $\varepsilon_{h\nu}$ are the limiting values of low and high frequency dielectric permittivities, respectively.

To check the results of our theory, we will conduct the experiments with uniaxial DFN, which provide the best manifestation of dielectric relaxation effects because a DFN has negative dielectric anisotropy for $\boldsymbol{\varepsilon}_f(t)$ and large positive contribution to the anisotropy from $\boldsymbol{\alpha}_s(t,t')$. In fact, in DFN the characteristic relaxation time $\tau_{\|}$ is much

larger than $\tau_{\perp}$, Table 1, so for our experiments we can assume that $\boldsymbol{\alpha}_s(t,t')$ contain only $\alpha_{\parallel}(t-t')$ component along the director:

$$\boldsymbol{\alpha}_s(t,t') = \alpha_{\parallel}(t-t')\mathbf{n}(t)\otimes\mathbf{n}(t'). \qquad (2.12)$$

The electric displacement $\mathbf{D}(t)$ can be written as,

$$\mathbf{D}(t) = \varepsilon_0\boldsymbol{\varepsilon}_f(t)\mathbf{E}(t) + \varepsilon_0\int_{-\infty}^{t}\alpha_{\parallel}(t-t')\mathbf{n}(t)\otimes\mathbf{n}(t')\mathbf{E}(t')dt'. \qquad (2.13)$$

where the fast permittivity tensor $\boldsymbol{\varepsilon}_f(t)$ reads,

$$\boldsymbol{\varepsilon}_f(t) = \varepsilon_{\perp}\mathbf{I} + (\varepsilon_{h\parallel} - \varepsilon_{\perp})\mathbf{n}(t)\otimes\mathbf{n}(t). \qquad (2.14)$$

Combine (2.2), (2.12) and (2.14), $\mathbf{D}(t)$ can be derived,

$$\mathbf{D}(t) = \varepsilon_0\mathbf{E}(t) + \varepsilon_0(\varepsilon_{h\parallel} - \varepsilon_{\perp})\big(\mathbf{n}(t)\cdot\mathbf{E}(t)\big)\mathbf{n}(t) + \varepsilon_0\frac{\varepsilon_{l\parallel} - \varepsilon_{h\parallel}}{\tau_{\parallel}}\int_{-\infty}^{t}\exp\left(-\frac{t-t'}{\tau_{\parallel}}\right)\big(\mathbf{n}(t')\cdot\mathbf{E}(t')\big)\mathbf{n}(t)dt'. \qquad (2.15)$$

The resulting dielectric torque density $\mathbf{M}(t)$ for the uniaxial NLC is:

$$\mathbf{M}(t) = \mathbf{D}(t)\times\mathbf{E}(t) = \varepsilon_0\mathbf{n}(t)\times\mathbf{E}(t)\cdot \left[(\varepsilon_{h\parallel} - \varepsilon_{\perp})\mathbf{n}(t)\cdot\mathbf{E}(t) + \frac{\varepsilon_{l\parallel} - \varepsilon_{h\parallel}}{\tau_{\parallel}}\int_{-\infty}^{t}\exp\left(-\frac{t-t'}{\tau_{\parallel}}\right)\mathbf{n}(t')\cdot\mathbf{E}(t')dt'\right]. \qquad (2.16)$$

The dielectric memory effect is described by the integral term of (2.16), which is absent in the standard approach. This integral term is called the memory torque, and the first term on the right hand side of (2.16) is called the instantaneous torque. Equation (2.16) holds for a liquid crystal with a Debye type of relaxation. It can be easily modified or generalized to other relaxation models (such as Cole-Davidson, Havriliak-Negami and other models with different functional forms of $\boldsymbol{\alpha}(t-t')$).

Equation (2.17) gives the standard dielectric torque representation, which is a special case of (2.16) by setting $\boldsymbol{\alpha}_s(t,t') = 0$,

$$\mathbf{M}(t) = \varepsilon_0(\varepsilon_{\parallel} - \varepsilon_{\perp})\mathbf{n}(t) \times \mathbf{E}(t) \cdot \left[\mathbf{n}(t) \cdot \mathbf{E}(t)\right]. \qquad (2.17)$$

2.2 Experiment and Analysis

To distinguish our model and the standard model and to verify the validity of our model, we need to maximize the dielectric memory term, i.e., the integral term in (2.16), since this integral term is absent in the standard model, (2.17). The orientational relaxation times of most typical NLCs, like 7CB, PAA, are less than 10^2 ns (Table 1), which increases the difficulty to observe the dielectric memory effect. In addition, for certain NLCs, such as 5CB, the ratio $\tau_{\parallel}/\tau_{\perp}$ is close to 1, which means the relaxations of $\varepsilon_{\parallel}$ and $\varepsilon_{\perp}$, to some extent overlap on in the same time scale. The overlapping of two relaxations further increases the difficulty to observe and analyze the memory effect.

An ideal material to study the dielectric memory effect is DFN material such as MLC2048 (EM industries, NY), due to its large relaxation time $\tau_{\parallel}$, and the large ratio $\tau_{\parallel}/\tau_{\perp}$. With the large $\tau_{\parallel}$ and the sign reversal of dielectric anisotropy $\Delta\varepsilon$, one can distinguish the contributions from instantaneous torque and memory torque in a relative large time scale. The large ratio $\tau_{\parallel}/\tau_{\perp}$ excludes the influence of the relaxation of $\tau_{\perp}$.

In section 2.2.1, we will discuss the molecular structure of DFN, the dielectric properties of DFN and the measurement technique.

In section 2.2.2, we will use electric field with different frequencies to drive DFN and discuss why the standard model (2.17) becomes invalid when the electric field changes abruptly.

2.2.1 Dual Frequency Nematic

As explained in section 1.4, DFN is a special NLC in which the dielectric anisotropy $\varepsilon_{\|}(f)-\varepsilon_{\perp}(f)$ changes sign from positive to negative as the frequency is raised through a cross-over frequency f_c [49-52].

From the molecular point of view, the DFN molecules have the strong dipole moment tilted from the long and short axis. DFN is of particular interest since $\Delta\varepsilon$ changes sign from positive to negative as the frequency raised through a crossover frequency f_c. The earliest DFN mixture is reported in 1974 [49] . Two nematogens are mixed at 1:1 concentration ratio to achieve the dual frequency properties, Figure 7. $\Delta\varepsilon$ changes from 6.1 (50 Hz) to -2.2 (10 kHz):

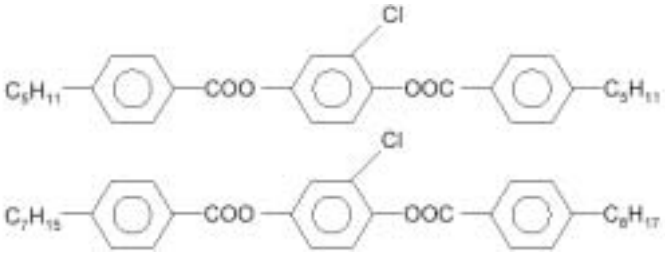

Figure 7. Two components of the earliest dual frequency liquid crystal mixture.

The property of the sign reversal of $\Delta\varepsilon$ of DFN provides a new possibility to switch the DFN in both ways rapidly by simply adjusting the driving scheme. DFNs have been successfully used for TN display [50-53], three dimensional display [54], polymer dispersed liquid crystal film [55-57], light shutters [58, 59], etc.

In the following part, we will explore the material properties of a typical DFN called MLC2048, such as dielectric permittivities, crossover frequency and rotational viscosity at different temperatures.

The dielectric permittivities of MLC2048 are measured by the capacitance method with its experimental setup shown in Figure 8.

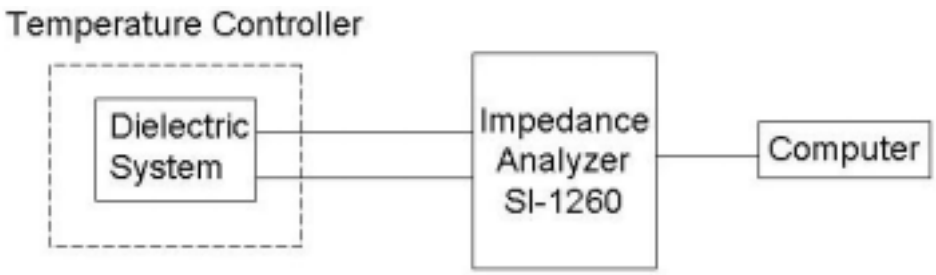

Figure 8. The setup of the capacitance method to measure the liquid crystal dielectric permittivity.

We used indium-tin-oxide (ITO) coated soda lime glass plates (Optera Colorado Inc.) to prepare the empty cells. The thickness of the empty cells was set at $d = 15 \pm 0.1\mu m$ by Mylar spacer. The inner surfaces of the glasses were coated with the aligning polyimide layers. We prepared two kinds of cells with planar and homeotropic orientation of

MLC2048. The planar alignment was provided by a rubbed layer of polyimide Dupont 2555, and the homeotropic alignment was achieved by coating with polyimide Nissan 7511. Before we fill the cell with MLC2048, the complex impedance amplitude $Z_e(f)$ of the empty cell were measured by Impedance/Gain-phase analyzer (model Schlumberger Solartron SI-1260) in the frequency range from 1 kHz to 1 MHz at voltage 0.5 V.

We then filled the cells with MLC2048, and mount the cell in a hot stage permitting temperature stabilization within 0.1 ^{0}C. The complex impedance amplitude $Z(f)$ of the cell were measured by SI-1260 impedance analyzer in the frequency range from 0.1 Hz to 1 MHz at voltage 0.5 V. The small voltage 0.5 V is chosen so as to avoid the director reorientation. Besides, the chosen low frequency range allows us to neglect the double-layer effect at the interfaces.

The equivalent circuits of the empty and filled cell are shown in Figure 9, in which R_{ITO} denotes the resistance of ITO electrodes, C_{Air} means the capacitance of the air inside the empty cell, C_{LC} and R_{LC} means the capacitance and resistance of the LC, respectively.

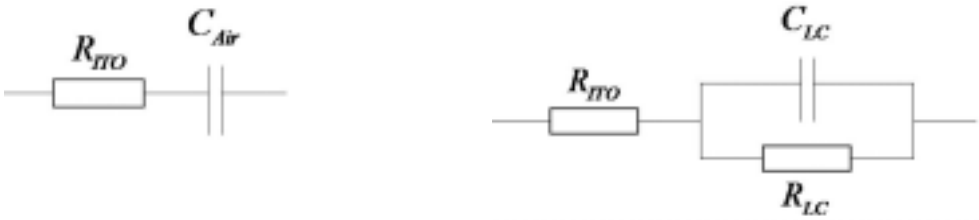

(a) (b)

Figure 9. The equivalent circuit of an empty cell, (a); and the cell filled with LC, (b).

For the homogeneous director field, we know that $C_{LC} = \varepsilon_0 \varepsilon_{LC}(f) A/d$, $R_{LC} = d/\sigma A$, where d is the cell thickness, A is the area of the electrodes, $\varepsilon_{LC}(f)$ is the frequency and orientation dependent permittivity of LC under test, $\sigma(f)$ is the frequency and orientation dependent electrical conductivity of the LC under test. For homeotropic alignment, we have $\varepsilon_{LC}(f) = \varepsilon_{\parallel}(f)$, $\sigma(f) = \sigma_{\parallel}(f)$; for planar alignment, we have $\varepsilon_{LC}(f) = \varepsilon_{\perp}(f)$, $\sigma(f) = \sigma_{\perp}(f)$.

Based on Figure 9(a), the impedance $Z_e(f)$ is

$$Z_e = R_{ITO} + \frac{1}{i2\pi f C_{Air}} = R_{ITO} + \frac{d}{i2\pi f \varepsilon_0 \varepsilon_{air} A}, \qquad (2.18)$$

where $\varepsilon_{air} = 1$ is the relative dielectric constant of air. When the applied frequency f is big enough, one can get the value of R_{ITO} from the measured Z_e directly, because $Z_e \to R_{ITO}$ at high frequencies. After we find R_{ITO}, we can then fit the experimental data with (2.18) to get an accurate ratio of d/A.

The impedance of the filled cell is

$$Z = R_{ITO} + \frac{1}{\frac{1}{R_{lc}} + i2\pi f C_{lc}} = R_{ITO} + \frac{d}{A} \frac{1}{\sigma(f) + i2\pi f \varepsilon_0 \varepsilon_{LC}(f)}. \qquad (2.19)$$

Although R_{ITO} and the ratio of d/A is already known from the impedance measurement of the empty cell, we still have two unknown frequency dependent variables, $\varepsilon_{LC}(f)$ and $\sigma(f)$. Strictly speaking, one cannot obtain $\varepsilon_{LC}(f)$ and $\sigma(f)$ simultaneously from eq. (2.19). However, the problem can be solved as follows. First

of all, we locate a frequency range, $[f_{\min}, f_{\max}]$, in which the phase angle of Z is very close to -90^0 (i.e., Z is a pure imaginary number). From (2.19), the pure imaginary number of Z means that the cell behaves as a capacitor so that we can neglect the contribution of R_{ITO} and R_{LC}. In our case with MLC2048, the frequency range in which the cell can be regarded as a capacitor is found to be [1kHz, 1MHz]. By fitting the experimental data with (2.19) in the above frequency range and with the assumptions $R_{ITO} = 0$ and $R_{LC} = \infty$, one can have the frequency dependent permittivity $\varepsilon_{LC}(f)$. $\varepsilon_{LC}(f = f_{\min})$ will be used for the next step to get $\sigma(f)$.

In the low frequency region, where neither the capacitance nor the resistance effect dominates, one can extract $\sigma(f)$ by using the fixed value $\varepsilon_{LC}(f_{\min})$ in (2.19). $\varepsilon_{LC}(f_{\min})$ is the low frequency dielectric constant obtained from the previous step.

Through the measurement, we found that the frequency dependence of dielectric permittivity for MLC2048 at 20^0C is well fitted by the Debye model [60] with $\varepsilon_{s\|} = 11.7$, $\varepsilon_{f\|} = 3.8$, $\tau_{\|} = 13.4\mu s$, as shown in Figure 10.

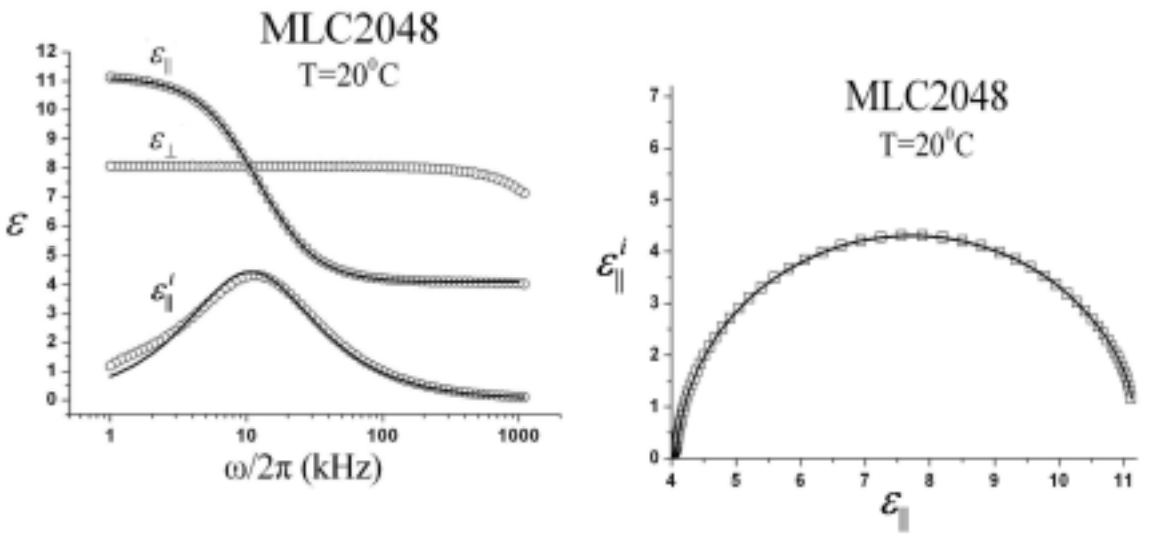

(a) (b)

Figure 10. (a) Frequency dependent dielectric permittivity $\varepsilon_{\parallel}$ and $\varepsilon_{\perp}$ of MLC2048 at $20^0 C$. The solid line is the fit of the experimental data with Debye equation $\varepsilon_{\parallel}^{*}(\omega) = \varepsilon_{f\parallel} + \frac{\varepsilon_{s\parallel} - \varepsilon_{f\parallel}}{1 + i\omega\tau_{\parallel}}$. (b) Cole-Cole plot for $\varepsilon_{\parallel}$ of MLC2048 at $20^0 C$; the experimental data (squares) are fitted with (1.26) very well, and form a Cole-Cole semicircle [61].

As Figure 10 indicates, the dielectric relaxation of $\varepsilon_{\parallel}$ in MLC2048 follows the model of a standard Debye relaxation. Correspondingly, the parallel component of the step response function $\alpha_{\parallel}$ reads

$$\alpha_{\parallel}(\omega) = \frac{\varepsilon_{s\parallel} - \varepsilon_{f\parallel}}{1 - i\omega\tau_{\parallel}}. \qquad (2.20)$$

Figure 11 demonstrates that the permittivities of MLC2048 are strongly temperature-dependent in the range of 20 ^{0}C to 40 ^{0}C, within the range of the nematic phase stability.

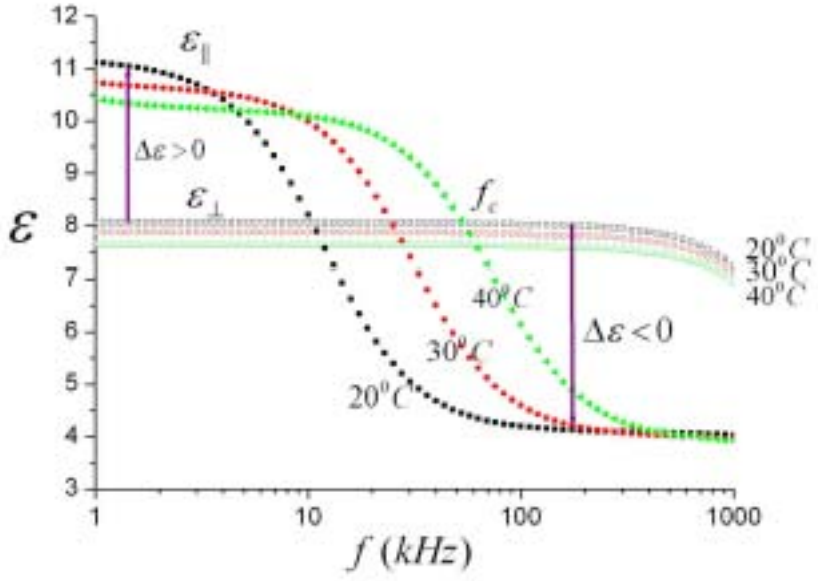

Figure 11. The $\varepsilon_{\parallel}, \varepsilon_{\perp}$ of MLC2048 at 20 ^{0}C , 30 ^{0}C, 40 ^{0}C.

The Nematic-Isotropic transition temperature of MLC2048 is 106 ^{0}C. We also measure $\Delta\varepsilon$ and f_c in the whole nematic range with 5 ^{0}C step, Figure 12.

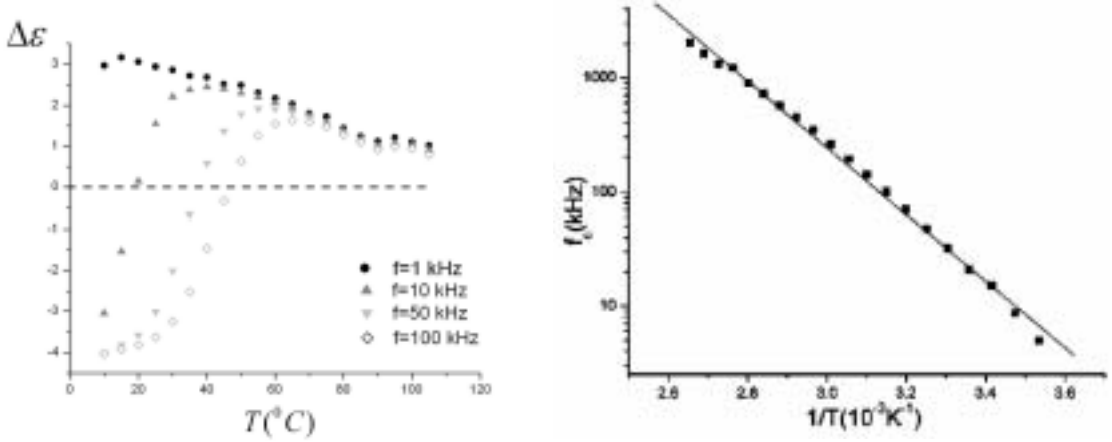

(a) (b)

Figure 12. The temperature dependencies of the dielectric anisotropy $\Delta\varepsilon$ (a), and the crossover frequencies f_c, (b), of MLC2048.

We notice that the cross-over frequency f_c increases with temperature, for example, from 12 to 61 kHz when T changes from 20 to 40 ^{0}C. At high temperature, $\Delta\varepsilon$ is always positive in a broad frequency range of applied voltage as shown in Figure 12(a). The temperature behavior of f_c can be fitted by a straight line in the inverse-logarithmic coordinates, Figure 12 (b), which implies that it is controlled by an activation process:

$$f_c \sim \exp(-E_f / k_B T), \qquad (2.21)$$

where k_B is the Boltzman constant and E_f is the activation energy representing the energy barrier associated with flip-overs of the long molecular axis. The linear fit in Figure 12(b) yields E_f = 0.61 eV.

2.2.2 Dielectric Memory Effect during the Switching

The competition between the instantaneous and memory contributions of the total torque in (2.16) determines the director dynamics. Note that the two coefficients, $(\varepsilon_{h\|} - \varepsilon_{\perp})$ and $(\varepsilon_{l\|} - \varepsilon_{h\|})$ in Eq. (2.16), can have *opposite* signs. It creates a very peculiar situation. Imagine now that the nematic id driven by a DC pulse. At zero frequency, the material is of a positive dielectric anisotropy. Anisotropy and the director should reorient parallel to the field. However, if the DC pulse has a very sharp profile with a large increase rate, then the response of the director would be opposite to what is expected. Namely, the sharp front would be perceived as a high-frequency field and the director might turn perpendicular to the field, at least at the beginning of the applied voltage pulse.

This curious situation might seriously delay the response time of the nematic LC in practical devices and, what is interesting; it cannot be grasped by the classic instantaneous model of the electrooptic response. .

To test whether this unusual scenario of the director reorientation in the sharply increased field, namely, initial orientation perpendicular to the field with a subsequent reorientation along the field, is really taken place, we designed a special experiment. We traced the director dynamics by measuring the optical phase retardation of the cell filled with MLC2048. To maximize the dielectric torque, we choose the geometry in which the initial director is tilted by an angle $\theta_0 \sim 45^0$ with respect to the bounding glass plates. The high pretilt alignment is realized by the deposition of the SiO layer. The cell thickness is $10\mu m$.

The cell is thermo-stabilized at $20 \pm 0.1^0 C$ and placed between two crossed polarizers in such a way that the director projection onto the glass plates makes an angle 45^0 with the polarization axes. The cell is driven by the electric pulses with modulated amplitude and frequency using the waveform generator WFG 500 (FLC Electronics Inc). The electric field reorients the director which is manifested by the change of the optical phase retardation $\Delta\varphi$ between the extraordinary and ordinary waves. The latter, in its turn, changes the measured intensity $I \propto \sin^2(\Delta\varphi/2)$ of light transmitted through the cell and the pair of crossed polarizers. The transmitted light (we used He-Ne laser, $\lambda = 633$ nm) intensity is measured by the photo diode and analyzed by an oscilloscope (Tektronix

TDS 210). The instruments allow us to detect processes with the time resolution of 1 μs or better.

Figure 13 shows the transmitted intensity (top trace) versus the applied voltage (bottom traces) at two frequencies (100 kHz and 1 kHz) when the amplitude of the voltage varies slowly with the rate 2.4 V/s. For such a slow rate, the dielectric behavior of DFN can be regarded as a quasi-static dielectric response, where the standard description with an instantaneous relation between the displacement and the field is valid.

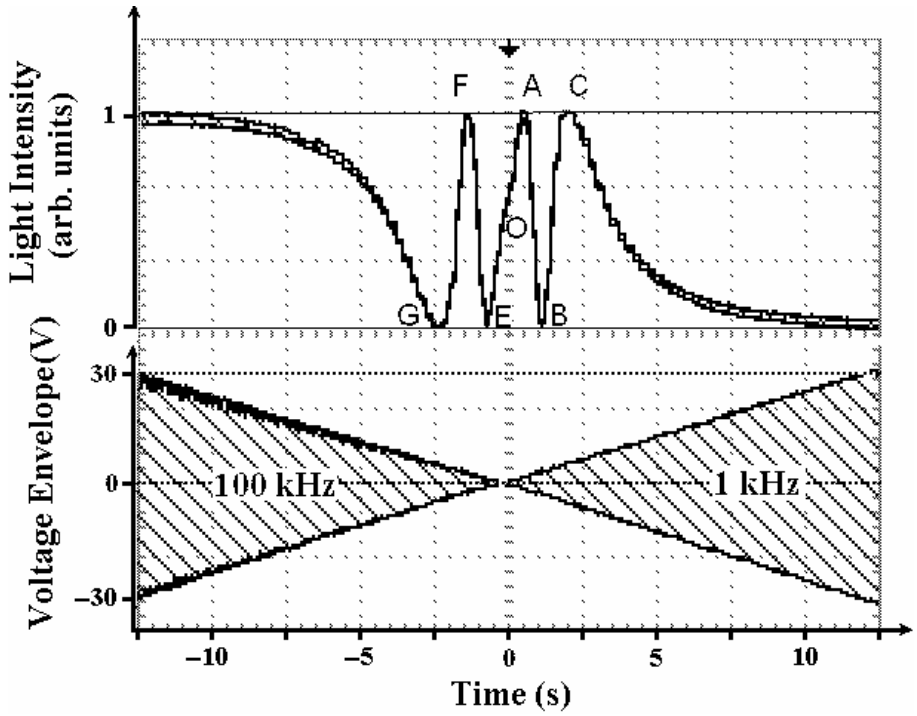

Figure 13. Transmitted light intensity modulated by the changes of optical retardation (top curve) vs. slowly changing voltage (bottom trace) applied at two different frequencies 100 kHz (left part) and 1 kHz (right part) to the MLC2048 cell of thickness d=10 μm. Point "O" corresponds to light transmittance at zero voltage.

The dielectric memory effect described by the last term in (2.16) becomes evident when the voltage changes abruptly. The behavior of light intensity recorded for 100 kHz pulses in Figure 14(a) is in agreement with the quasi-static behavior in Figure 13. However, the initial response to a step-like pulse of a low frequency, Figure 14(b), is exactly opposite to what is expected from the quasi-static model and experiment in Figure 13. Namely, Figure 13 suggests that the light intensity should increase when the voltage is increased at 1 kHz, while Figure 14(b) demonstrates that the voltage pulse actually decreases the light intensity (towards point Y in Figure 14(b)) at the beginning of director reorientation. This anomalous decrease is not related to the possible parasitic effects such as light scattering losses: The insert in Figure 14(b) demonstrates that the trend is reversed when an additional π phase retarder (Soleil-Babinet compensator SB-10 purchased from Optics for Research) is inserted between the cell and the polarizer. Therefore, the reason for the different response of the director to the quasi-static, Figure 13, and abrupt, Figure 14(b), voltage increase at 1 kHz is not related to the parasitic effects and might be caused by the dielectric memory effect, i.e., by the fact that $\mathbf{D}(t) \neq \varepsilon_0 \boldsymbol{\varepsilon} \mathbf{E}(t)$.

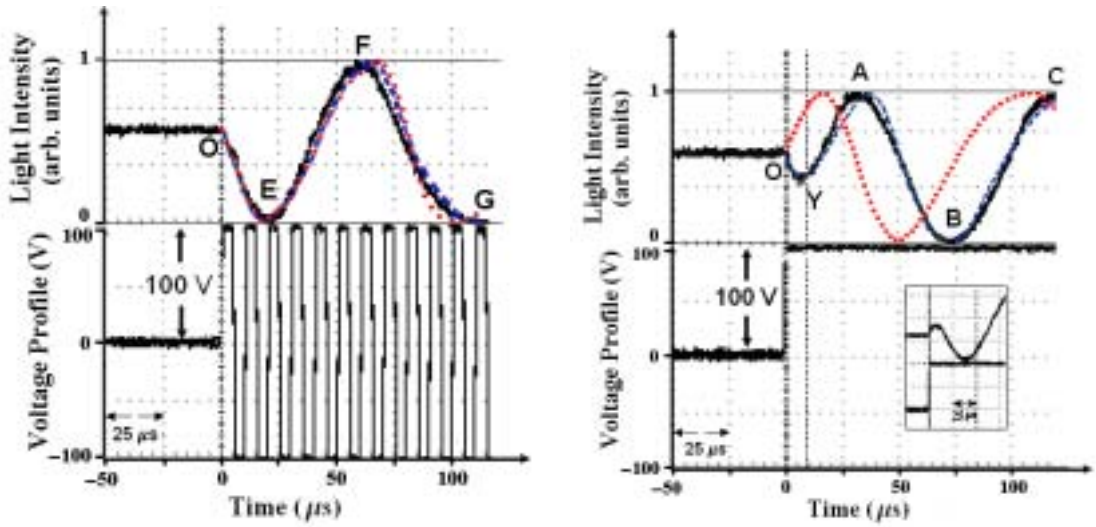

(a) (b)

Figure 14. Transmitted light intensity modulated by the changes of optical retardation for the same DFN cell as in Figure 13, but driven by steep changes of the applied voltage at 100 kHz (a) and 1 kHz (b). The voltage profile is shown by the lower traces. The time scale is 25 μs/sqr. In the top parts, the solid lines are the oscilloscope's trace for the experimentally determined light transmittance, the dashed lines represent the transmitted intensity as calculated from our model, and dotted lines represent the standard approach with $\mathbf{D}(t) = \varepsilon_0 \boldsymbol{\varepsilon} \mathbf{E}(t)$. The insert in part (b) is the optical transmission for the DFN cell driven by a 1 kHz pulse when a π phase retarder is inserted between the polarizer and the cell.

To verify our model, Eq. (2.16), we simulated the transmitted light intensity using (2.16). The polar angle $\theta(z,t)$ between **n** and the normal to the cell is described by (2.22):

$$-\gamma_1 \frac{\partial \theta}{\partial t} = M(t) - \left[K_{11} \sin^2 \theta(z,t) + K_{33} \cos^2 \theta(z,t) \right] \frac{\partial^2 \theta(z,t)}{\partial z^2}, \qquad (2.22)$$

where γ_1 is the rotational viscosity, $M(t)$ is the magnitude of the dielectric torque, K_{11}, and K_{33} are the elastic constant for splay and bend deformations of the NLC, respectively. We neglect the backflow effects as we are interested in the very beginning of field-induced reorientation; the initial condition is $\theta(z, t=0) = \theta_0 = 45^0$ at $M(t=0) = 0$. The optical phase shift is calculated as

$$\Delta\varphi = \frac{2\pi n_o}{\lambda} \int_0^d \left(\frac{n_e}{\sqrt{n_o^2 \sin^2 \theta(z,t) + n_e^2 \cos^2 \theta(z,t)}} - 1 \right) dz . \qquad (2.23)$$

To compare the model and the experiment, we independently measured the rotational viscosity and elastic constants of MLC2048: $\gamma = 0.3\,\mathrm{kg\,m^{-1}\,s^{-1}}$ using the technique described in Ref [44], and $K \doteq 20\,\mathrm{pN}$, the cell thickness $d = 10\,\mu\mathrm{m}$; the extraordinary and ordinary indices of refraction: $n_e = 1.705$ and $n_o = 1.495$ (both at $\lambda = 633\mathrm{nm}$).

The experimental light intensity curves in Figure 14 are compared to the two models: the model developed in this work (2.12)-(2.16) (dashed lines), and the standard model (dotted lines) with an instantaneous relationship $\mathbf{D}(t) = \varepsilon_0 \boldsymbol{\varepsilon} \mathbf{E}(t)$. The new model agrees well with the experiment, while the standard model contradicts it. The standard model, as compared with the experiments, shows the opposite directions of intensity changes and thus the opposite direction of the director reorientation when the amplitude of 1 kHz voltage changes abruptly [Figure 14(b)]. When the voltage amplitude increases slowly, as in Figure 13, the difference in the new and standard approaches vanishes.

In Figure 15, we choose the points O, Y, A and B of Figure 14(b) and calculate how the polar angle $\theta(z,t)$ changes using (2.22). Figure 15 demonstrates how the director experiences a reverse rotation toward $\mathbf{n} \perp \mathbf{E}$ near $t = t_Y$, and then reorient in the direction $\mathbf{n} \parallel \mathbf{E}$.

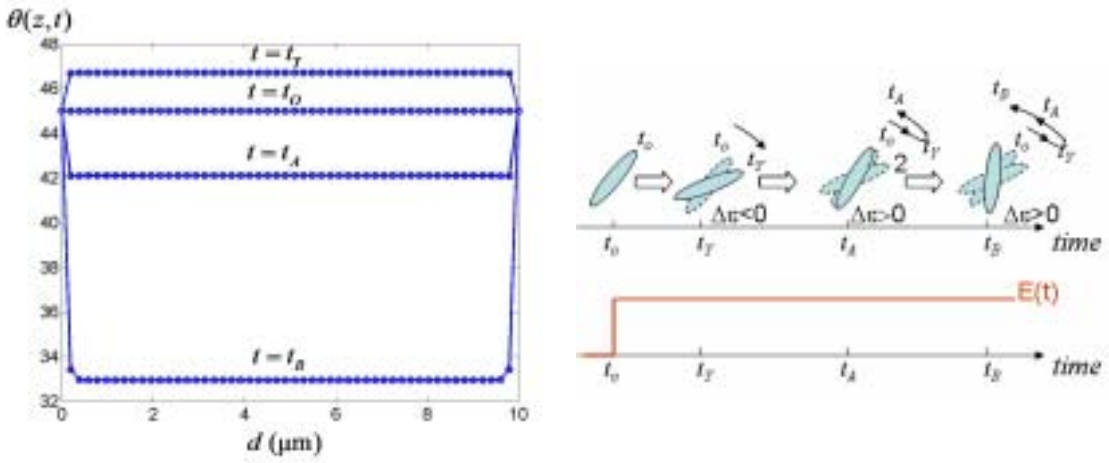

(a) (b)

Figure 15. (a) The simulation of the polar angle $\theta(z,t)$ of the points of O, Y, A and B of Figure 14(b). (b) The demonstration of the director reorientation of the MLC2048 cell at O, Y, A and B. The director reorients in the direction of $\mathbf{n} \perp \mathbf{E}$ because the memory torque dominates when $t \in [t_o, t_Y]$. During the period $[t_Y, t_B]$, the instantaneous torque dominates, therefore, the director reorients in the direction of $\mathbf{n} \parallel \mathbf{E}$.

Is there any experimental evidence that the phenomenon of non-instantaneous relationship between the displacement $\mathbf{D}$ and the electric field $\mathbf{E}$ can indeed be relevant in regular NLCs? Some time ago, N. Clark's group demonstrated that the typical nematic

material pentylcyanobiphenyl (5CB) can be switched very quickly, within a few tens of nanosecond, if the applied voltage is large (hundreds of volts) [9]. According to the dielectric spectroscopy data [45, 62], this switching time is in fact of the same order as τ for 5CB, which might suggest that the NLC response is influenced by the dipole relaxation dynamics. Further research needs to be done to verify the validity of our model in typical NLCs.

2.3 Conclusions

To conclude this chapter, we demonstrated that the widely accepted model of the instantaneous relationship between the electric displacement and the electric field in the NLC is invalid when the characteristic times of the director dynamics are close to the relaxation times for molecular permanent dipoles. This time scale for dual-frequency nematic materials is typically in the submillisecond range, which is of great interest for modern fast-switching devices. We propose a general model to quantitatively describe the orientation dynamics of dispersive liquid crystals in which the assumption of the instantaneous relationship between the electric displacement and the electric field is lifted. The dielectric permittivity tensor of the reorienting liquid crystal is no longer constant during the switching process. The proposed model expresses the electric displacement $\mathbf{D}(t)$ (as well as the dielectric torque density $\mathbf{M}(t)$) as the function of the static dielectric properties of the NLC, the present and past electric field, and the present and past director.

The model allows us to describe quantitatively the processes of fast switching in the submillisecond range. We verified the prediction of the model experimentally, using the dual-frequency nematic MLC2048; similar results were also obtained for another DFN material, Rolic 2F-3333 (Rolic Ltd). In this work, we employ a simplified hydrodynamic approach neglecting the backflow effects. The approach is justified, as the region between points *Y* and *O* in Figure 14(b), where the difference between the experiment and the standard theory is most evident, corresponds to a phase change of about 1 rad and thus to a relatively small reorientation of **n**, by about 3^0. However, should the complete set of hydrodynamic equations be needed for the description of fast director reorientation, it should include the dielectric torque description proposed here. The proposed model should be applicable to dynamic reorientation of other LC phases; the model might involve not only the director but also the scalar order parameter. In the case of ferroelectric LCs, the theory should be supplemented by the consideration of spontaneous electric polarization. A similar approach should be also applied to other systems, including those of biological significance, with tensor order parameters and nonstationary dielectric properties.

Chapter 3

ELECTRIC HEATING OF NEMATIC LIQUID CRYSTAL CELL

There are two important general consequences of the dielectric relaxation phenomena: (1) nonlocal time relationship between the electric displacement $\mathbf{D}(t)$ and the electric field $\mathbf{E}(t)$ and (2) dielectric heating. The first effect is a reflection of the fact that $\mathbf{D}(t)$, being a function of both $\mathbf{E}(t)$ and the material's dielectric properties, needs some finite time to adjust the value of the electric field, which has been analyzed systematically in chapter 2. The second effect, dielectric heating, is related to the efficiency of the absorption of electromagnetic energy by the dielectric medium through reorientation of the molecular dipoles and associated molecular frictions. This absorption is small when the frequency of the applied field is low and smaller than the dielectric relaxation, but it becomes very efficient in the region of dielectric relaxation.

In this chapter, we explore the electric heating effects of NLC cells in an AC electric field caused by the dielectric relaxation and by the ionic currents of the NLC (although the latter can be neglected at field frequencies higher than a few kilohertz).

In section 3.1, we propose a theoretical model that incorporates the finite thermal conductivity of the bounding plates. The model shows how the temperature dynamics

and the stationary value of the temperature increase depend on the parameters of the materials and the applied field.

In section 3.2, the experiments confirm the theoretical predictions, such as that the temperature rise is controlled not only by the heat transfer coefficient of the surrounding medium but also by the thickness and the thermal conductivity coefficient of the bounding plates and director orientation. To study the temperature dynamics experimentally, we use a tiny E-type thermocouple (Newport Electronics, CHCO-0005) with the head size of 25 μm inserted directly into 40 μm thick NLC slab. We verify that the presence of thermocouple does not affect the thermal behavior of the sample by comparing the data to data obtained with the noncontact birefringence technique [47] for the case. We perform experimental studies for a variety of surrounding media with different heat transfer properties (from extremely good heat conductors such as aluminum cooling device to extremely poor conductor, Styrofoam) and for different frequencies of the applied field, including those that correspond to different regions of dielectric relaxation.

3.1 Model

Electric heating effects in the NLC change the LC physical properties and dynamics. In this section, we propose a model to quantitatively describe the heating

effect caused by dielectric dispersion as well as ionic conductivity in the NLCs upon the application of an AC electric field.

When a nematic cell is driven by a harmonic electric field $\mathbf{E} = \mathbf{E}_0 \cos 2\pi ft$, the heating power density P caused by the dielectric relaxation and the ionic current in NLC can be written as:

$$\mathbf{P}_h = f\int_0^{1/f} \mathbf{E}\left(\frac{\partial \mathbf{D}}{\partial t} + \mathbf{J}\right)dt = \pi f \varepsilon_0 \mathbf{E}_0 \cdot \varepsilon^i \cdot \mathbf{E}_0 + \frac{1}{2}\mathbf{E}_0 \cdot \boldsymbol{\sigma} \cdot \mathbf{E}_0, \qquad (3.1)$$

where $\mathbf{J}$ is the current density, $\boldsymbol{\sigma}$ is the conductivity tensor of the NLC. The tensor $\boldsymbol{\sigma}$ and $\boldsymbol{\varepsilon}$ and thus heating power density $\mathbf{P}_h$ depend on the orientation of the NLC director $\mathbf{n}$. In what follows, for the sake of simplicity, we assume that the electric field is homogeneous inside the cell. Therefore, one can represent the electric field through the applied voltage U acting across a NLC cell of a thickness d, $\mathbf{E}_0 = \frac{U}{d}\hat{\mathbf{z}}$, so that

$$P_h = \frac{\pi f \varepsilon_0 \varepsilon_{zz}^i U^2}{d^2} + \frac{\sigma_{zz}^i U^2}{2d^2}, \qquad (3.2)$$

where $\varepsilon_{zz}^i = \varepsilon_\perp^i \sin^2\theta + \varepsilon_\parallel^i \cos^2\theta$ is the imaginary part of the effective dielectric permittivity, $\sigma_{zz}^i = \sigma_\perp^i \sin^2\theta + \sigma_\parallel^i \cos^2\theta$ is the effective ionic conductivity of the material, and θ is the angle between the director $\mathbf{n}$ and the normal $\hat{\mathbf{z}}$ to the bounding plates.

Let us discuss now the scheme of the dielectrically-induced heat production and its transfer in the multilayered system comprised of an NLC layer, two bounding plates of finite thickness (but of infinite size in the two other directions), placed into some surrounding medium of infinite extension, Figure 16.

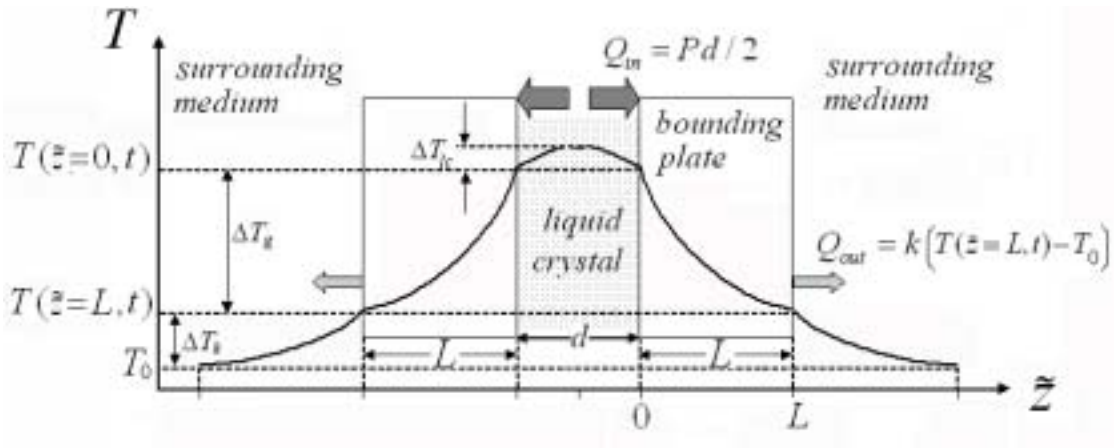

Figure 16. The scheme of the dielectric heating of an NLC cell.

The heat conduction equation for each of the layers is of a generic form [63]:

$$c_p \rho \frac{\partial T(z,t)}{\partial t} = G \frac{\partial^2 T(z,t)}{\partial z^2} + P_0 , \qquad (3.3)$$

where c_p is the heat capacity of the layer, ρ is the material density, G is the layer's thermal conductivity, P_0 is the specific heat production inside the layer. Equation (3.3) should be accompanied with the boundary conditions that guarantee the heat flow balance.

For the case of the NLC layer, $P_0 = P_h$. The temperature drop across the NLC slab is maximum for a stationary regime. Equation (3.3) allows us to estimate the temperature drop as $\Delta T_{LC}(t) \le Pd^2/8G_{LC} = (2\pi f \varepsilon_0 \varepsilon_{zz}^i + \sigma_{zz})U^2/16G_{LC}$, where G_{LC} is the thermal conductivity of the liquid crystal. For a typical situation, $G_{LC} \approx 0.2 \mathrm{Wm^{-1}K^{-1}}$ [64], $\varepsilon_{zz}^i \approx 1$, $U \le 50\mathrm{V}$, $f \le 10^6 \mathrm{Hz}$, the temperature drop is only of the order of $0.05^0 C$. Therefore, we can assume that the temperature drop across the (relatively thin) NLC layer is small and concentrate on the temperature changes in the bounding plates.

In what follows, we consider the system being symmetric with respect to the middle plane of the NLC cell and apply (3.3) to describe the heat conduction through one of the two bounding plates, for example, the one located within $z \in [d/2, d/2+L]$ or $\tilde{z} \in [0, L]$, where $\tilde{z} = z - d/2$ is introduced to simplify the notations. Equation (3.3) needs to be supplemented by two boundary conditions for the heat transfer, at the NLC-bounding plate interface and at the bounding plate-surrounding medium interface. Because the NLC layer is thin as compared to the bounding plates, one can neglect the heat stored in the NLC layer itself, so that the heat flux from the NLC layer to the bounding plate is $Q_{in} = Pd/2$. We assume that the heat flux Q_{out} at the bounding plate-surrounding medium interface obeys the Newton's cooling law, i.e., $Q_{out} = k[T(\tilde{z} = L, t) - T_0]$, where $T(\tilde{z} = L, t)$ is the temperature of the plates outer boundary, T_0 is the temperature of the surrounding medium at infinity, and k is the heat transfer coefficient of the surrounding medium. The boundary conditions are then written as:

$$\frac{\partial T(\tilde{z}=0,t)}{\partial z} = -\frac{Pd}{2G}, \qquad \frac{\partial T(\tilde{z}=L,t)}{\partial z} = -\frac{k}{G}[T(\tilde{z}=L,t) - T_0], \tag{3.4}$$

where $T(\tilde{z} = 0, t)$ is the temperature of the NLC-bounding plate interface.

The solution $T(\tilde{z}, t)$ of (3.3), supplemented with the boundary conditions in (3.4) and the initial condition $T(\tilde{z}, t = 0) = T_0$, is

$$T(\tilde{z},t) = T_0 + \Delta\bar{T}_k \left[1 + Bi\left(-\frac{\tilde{z}}{L} + 1 \right) - \sum_{n=1}^{\infty} a_n \cos q_n \frac{\tilde{z}}{L} \exp\left(-\frac{t}{\tau_n} \right) \right], \tag{3.5}$$

where $\Delta\bar{T}_k = \dfrac{\left(2\pi f \varepsilon_0 \varepsilon_{zz}^i + \sigma_{zz}\right)U^2}{4kd}$ is the characteristic temperature drop, as we shall see later, $\Delta\bar{T}_k$ is the stationary value of the temperature difference between the bounding plate's external boundary $\tilde{z} = L$ and the point $\tilde{z} \to \infty$ in the surrounding medium. The constant $Bi = kL/G$ is called the Biot number [65], $a_n = 2\tan q_n / (\sin q_n \cos q_n + q_n) > 0$ are the dimensionless coefficients with the eigenvalues q_n satisfying the equations $q_n \tan q_n = Bi$, and $\tau_n = c_p \rho L^2 / G q_n^2$ are the characteristic time constants determining the transition to the stationary regime. For the convenience of further analysis, we will consider the temperature change $\Delta T(t)$ of NLC measured as the difference between the temperature T_0 of the NLC bulk and the temperature at infinity $\tilde{z} \to \infty$ (which is also the initial temperature of the whole system),

$$\Delta T(t) = \Delta T_k \left[1 + Bi - \sum_{n=1}^{\infty} a_n \exp\left(-\frac{t}{\tau_n}\right)\right], \qquad (3.6)$$

as the sum of the following two contributions:

$$\Delta T(t) = \Delta T_k(t) + \Delta T_g(t), \qquad (3.7)$$

where

$$\Delta T_k(t) = \Delta\bar{T}_k \left[1 + Bi - \sum_{n=1}^{\infty} a_n \cos q_n \exp\left(-\frac{t}{\tau_n}\right)\right] \qquad (3.8)$$

is the difference between the temperature $T(\tilde{z} = L, t)$ of the bounding plate's external boundary and T_0, and $\Delta T_g(t) = T(\tilde{z} = 0, t) - T(\tilde{z} = L, t)$ is the temperature difference across the bounding plate, Figure 16.

As one can see from Eqs (3.5)-(3.8), the stationary value $\Delta T_k(t \to \infty)$ is indeed equal to ΔT_k; besides, $\Delta T_g(t \to \infty) = \Delta \overline{T}_g = Bi \Delta \overline{T}_k$. Therefore, the temperature increase of the NLC slab, $\Delta \overline{T} = \Delta T(t \to \infty)$, can also be represented by the sum of two terms:

$$\Delta \overline{T} = \Delta \overline{T}_k + \Delta \overline{T}_g = \frac{\left(2\pi f \varepsilon_0 \varepsilon_{zz}^i + \sigma_{zz}\right) U^2}{4kd}(1 + Bi). \qquad (3.9)$$

The model above, Eq. (3.9), suggests that one can distinguish two regimes of electric heating. When $Bi >> 1$, the temperature increase of the NLC is controlled mainly by the temperature gradient in the bounding (glass) plates. For $Bi << 1$, the dominating control parameter is the heat transfer coefficient k of the surrounding medium, $\Delta \overline{T} \approx \Delta \overline{T}_k$. Equations (3.5)-(3.9) indicate that the NLC temperature change is influenced by many factors, including the LC's imaginary dielectric permittivity components ε_{zz}^i, electric conductivity σ_{zz}, electric field (voltage U and frequency f), thermal properties of the surrounding medium (heat transfer coefficient k), and properties of the bounding plates (thermal conductivity G, heat capacity c_p, and thickness L).

3.2 Experiment and Analysis

Indium-tin-oxide (ITO) coated soda lime glass plates (Optera Colorado Inc.) of the thickness L=1.1 mm are used to make the liquid crystal cell. The glass parameters are as follows: c_p =840 J kg^{-1} K^{-1} [66], ρ =2.44×10^3 kg m^{-3} [67, 68], G =0.94 W m^{-1} K^{-1} [68].

To measure the liquid crystal temperature, we inserted a tiny ($25\mu m$) Chromega-Constantan thermocouple into the liquid crystal bulk. To avoid an electric contact of the thermocouple and ITO, we spin coated a thin ($1\ \mu m$) electric insulating layer (Nissan AT-720A) onto ITO. The layer is thin enough to cause no effect on the AC component of the field and the temperature gradients in the system. The reference end of the thermocouple is placed in the surrounding medium with temperature T_0, which is close to 23 ^{0}C. The measured NLC temperature data were transferred from the i-8 thermometer (Newport Electronics Inc.) to the computer through the RS-232 interface (Figure 17).

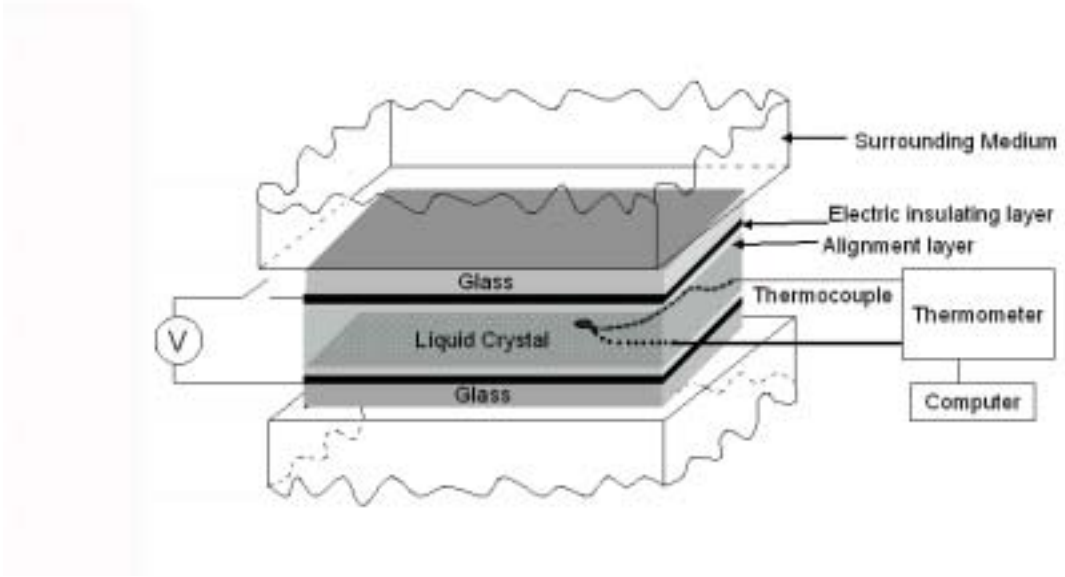

Figure 17. Experimental setup to measure the temperature of the nematic cell driven by the electric field.

The glass plates were additionally coated with the aligning layers of a rubbed polyimide (Dupont 2555) to set a uniform unidirectional orientation of the director in the plane of the substrates. The cell thickness was set at $d = 40\mu m$ by Mylar stripes. The

lateral size of the cells was 2 × 2 cm^2 with the head of the thermocouple placed in the center.

The cell was filled with MLC2048. The case of DFNs is of special interest in our studies. In these materials, the real part of the dielectric anisotropy $\Delta\varepsilon(f)$ changes its sign from positive at $f < f_c$ to negative at $f > f_c$. From Chapter 2 and section 3.1, the crossover frequency f_c usually corresponds to the region of dielectric relaxation of $\varepsilon_{\|}(f)$ with a characteristic time $\tau_{\|}$, $f_c \approx (2\pi\tau_{\|})^{-1}$, and to the maximum of the dielectric heating. Typically, f_c is low, in the range from 1 kHz [69] to 1 MHz [70], which is the range in which most electric driving schemes are operating. For MLC2048, f_c = 15 kHz at 23 ^{0}C. The DFNs are usually formed by mixtures with molecules that have significant permanent dipole moments; therefore, the dielectric heating effects are well pronounced. Furthermore, the sign reversal of the dielectric anisotropy at f_c makes it possible to study the role of different components of the dielectric tensor on the dielectric heating phenomenon (when $f < f_c$, the director aligns parallel to the applied field and perpendicular to it when $f > f_c$). The dielectric heating in DFNs is also important because f_c and other material parameters of these materials are strongly temperature dependent. Finally it is important to bear in mind that many conventional NLCs are actually DFNs at sufficiently high frequencies. For example, in the most popular nematic material pentylcyanobiphenyl (5CB), $f_c \approx 20$MHz [71], while in hetylcyanobiphenyl (7CB), $f_c \approx 9$MHz [72] (both measured at room temperature).

To check whether the thermocouple affects the thermal behavior of the NLC cell or not, we compare the temperature data read from thermocouple and the temperature data obtained from the noncontact birefringence technique proposed by Wen and Wu [47]. The working principle of the birefringence method is described briefly as follows. The light transmission intensity of a nematic cell with uniform alignment placed between two crossed polarizers can be written as

$$I = I_0 \sin^2 2\varphi_0 \sin^2(\Delta\Phi/2) \qquad (3.10)$$
$$= I_0 \sin^2 2\varphi_0 \sin^2\left[\frac{\pi d}{\lambda}\left(\frac{n_o n_e}{\sqrt{n_e^2\cos^2\theta + n_o^2\sin^2\theta}} - n_o\right)\right],$$

where φ_0 is the angle between the projection of the director **n** in the azimuthal plane and polarization of the incident light. If the cell keeps the strict planar alignment during the whole period, $\theta = \pi/2$, one can obtain how the birefringence $\Delta n = n_e - n_o$ changes with time by recording the transmitted light intensity $I(t)$, Eq. (3.11),

$$\Delta n(t) = \frac{\lambda}{\pi d}\left\{k\pi \pm \arcsin\left[\sqrt{I(t)/I_0 \sin^2 2\theta}\right]\right\}. \qquad (3.11)$$

The temperature $T(t)$ at the moment t therefore can be derived once Δn as a function of the temperature T is identified. We use Abbe refractometer to measure the birefringence Δn of MLC2048 at a broadband range of temperatures (20–70 °C) and polynomially fit Δn as a function of T, Figure 18.

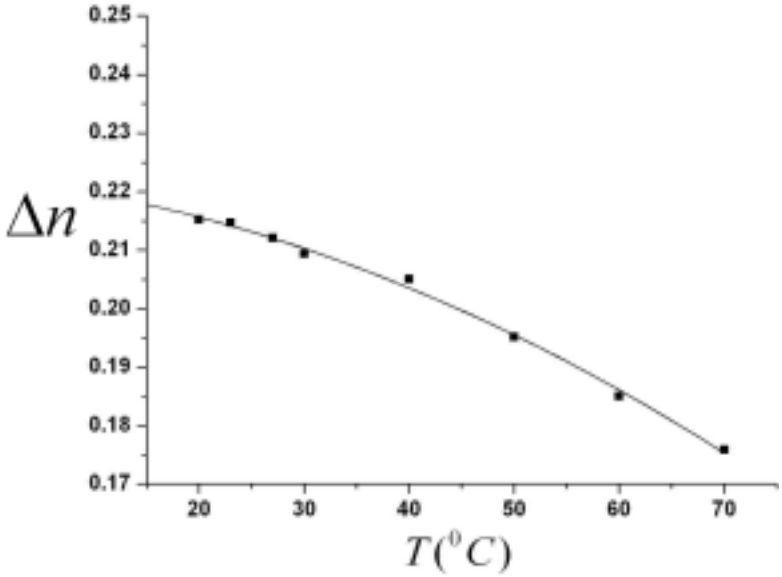

Figure 18. Temperature dependence of birefringence Δn for MLC2048. The squares are the measured values, and the solid line is the polynomial fitting line, $\Delta n = \Delta n_0 + a(T-20) + b(T-20)^2$, where $\Delta n_0 = 0.216$, $a = -0.0047$, and $b = -6.8054 \times 10^{-6}$. The accuracy of the birefringence measurement is ±0.001.

To trace the birefringence dynamics $\Delta n(t)$, we measured the transmission light intensity of the 40 μm planar MLC2048 cell. The cell is thermally stabilized at 23 ± 0.1 °C and placed between two crossed polarizers in such a way that the director projection onto the glass plates makes an angle 45° with the polarization axis, i.e., θ =45°. The cell is driven by the harmonic electric fields produced by the DS345 wave form generator (Stanford Research System).

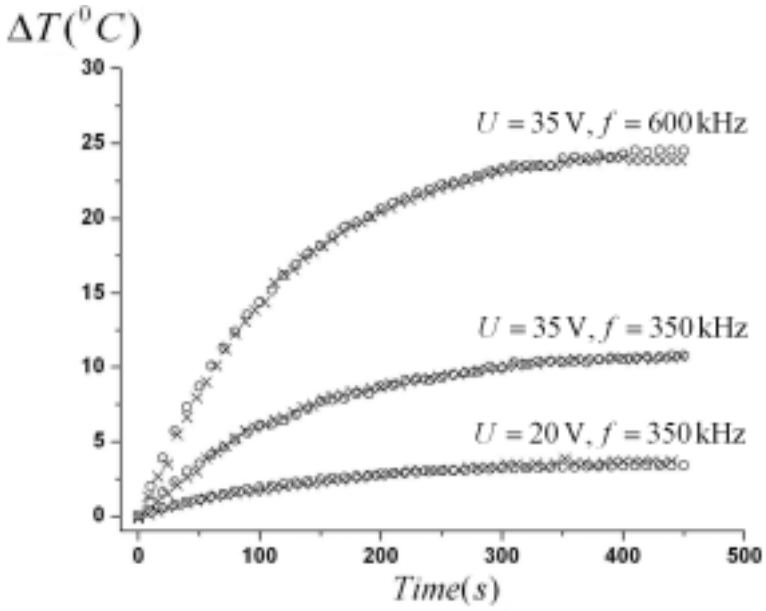

Figure 19. The LC temperature change $\Delta T(t)$ measured by two methods. The circles are the temperature data read from the thermocouple, and the cross symbols are from the noncontact birefringence method. The accuracy of the direct temperature measurement using the thermocouple is ±0.1 °C, while the birefringence approach gives ±0.5 °C.

Different electric fields are applied to the cell and the transmission light intensity change $I(t)$ is recorded and analyzed. The corresponding temperature $I(t)$ is derived by using (3.11) and $\Delta n(t)$ which is obtained by the fittings in Figure 18. Independently, we measured the LC temperature through the thermocouple, Figure 19. The comparison of both data sets in Figure 19 confirms that the finite thermocouple does not affect the thermal behavior of the NLC cell under test.

After we verified that the thermocouple do not affect the thermal behavior of the NLC cell, we want to examine how the different heat transfer coefficients *k* affect the dielectric heating-induced temperature rise of NLC. We used different surrounding

media, ranging from (1) aluminum cooling device, (2) circulating air, (3) still air, and (4) Styrofoam. In the experiment (1), we used the aluminum cooling devices P-2000 (Cyber Cooler, Inc.) composed of an aluminum radiator and a fan that are normally used as cooling fans for CPUs in computers. The NLC cell was sandwiched between the flat sides (lateral size of 2×2 cm^2) of the two devices with the fans switched on. To assure a good thermal contact between the glass and aluminum plates, we use a small amount of the thermal compound (Wakefield Engineering, Inc.) to fill the micro-gaps. In the experiment (2), the circulation of air was produced by the cooling fan P-2000 placed in such a way that the air flow was parallel to the surface of the NLC bounding plates. The distance between the cell edge and the fan was about 1 cm. In the experiment (3), the liquid crystal cell was hanged at two wires in the middle of the box with a size of $20 \times 20 \times 10$ cm^3 made of a plastic mesh with the mesh density of 36 cm^{-2} and the square opening size of 1 mm. The function of the plastic mesh is to restrict the convection of the air flow. Note that most experiments with LC cells in academic laboratories and industrial devices fall between (1) and (3) situations. In case (4), the cell was sandwiched between two Styrofoam plates with a thickness of 5 cm each.

Figure 20 illustrates the temperature dynamics caused by the electric heating effect for the planar NLC cell placed in four different surrounding media. The applied electric field ($U = 25\,\mathrm{V}$, $f = 500\,\mathrm{kHz}$) causes no director reorientation from the planar state. The temperature change is different in different media. First, the temperature change shows a tendency of saturation in media with good heat transfer (relatively high k). The

temperature increase is small for the cooled aluminum surrounding and then increases in circulating and still air, which is a naturally expected result. For Styrofoam with poor heat transfer, the temperature increase is the largest and is not showing clear signs of saturation, at least within the time of experiment, Figure 20.

Note that at the high frequencies used in our experiment, the electric heating effect is caused essentially by the dielectric mechanism. The Ohmic heating $P_\sigma = \sigma U^2 / 2d^2$ of the ionic current is negligibly small as compared to the dielectric heating because for the typical conductivity $\sigma \sim 10^{-9}\Omega^{-1}m^{-1}$, the ratio of the conductive heating to the dielectric heating, $P_\sigma / P = \sigma / \pi f \varepsilon_0 \varepsilon_{zz}^i$, is very small, less than 0.01, when $f > 3\text{kHz}$. Therefore, in what follows, we will refer to the electric heating effect as to the dielectric heating effect.

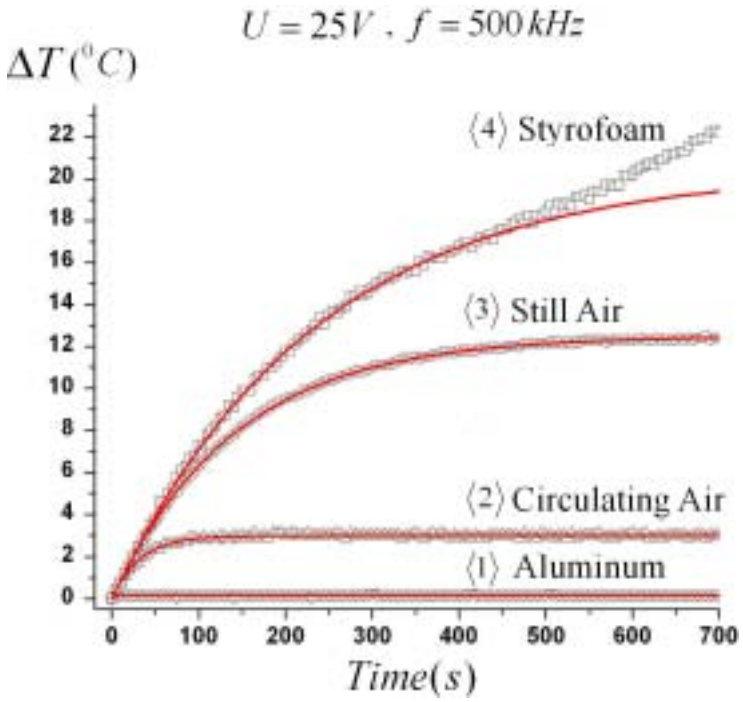

Figure 20. Measured temperature change of the MLC2048 cell as a function of time surrounded by media (a) to (d). The red solid lines are the fits of the experimental data with Eq. (8). The surrounding and initial temperature is $T_0 = 23^0 C$. The electric field frequency is 500 kHz, and the voltage amplitude is 25V.

Theoretically, Eq. (3.6), the NLC temperature increase $\Delta T(t)$ depends on series, $a_n \exp(-t/\tau_n)$. The first term n=1 in this series is dominant, because of the two reasons. First, the characteristic times $\tau_n = c_p \rho L^2 / G q_n^2$ with n>1 are at least nine times smaller than τ_1 and shorter than 0.3 s. Really, by using c_p=840 J kg^{-1} K^{-1} [66], ρ=2.44×10^3 kg m^{-3} [67, 68], and G=0.94 W m^{-1} K^{-1} [68], one finds $\tau_n = 2.6/q_n^2$ s; since $q_n > (n-1)\pi$, the largest relaxation time with n>1 is thus τ_2<0.3 s. Second, the first amplitude a_1 is at

least six times larger than the sum of the amplitudes of all other terms. Equation (3.6) is then simplified to

$$\Delta T(t) = \Delta \overline{T}\left[1 - \exp\left(-\frac{t}{\tau_1}\right)\right], \qquad (3.12)$$

where

$$\tau_1 = \frac{c_p \rho L^2}{G q_1^2}. \qquad (3.13)$$

Equation (3.12) describes the experimentally observed temperature dynamics for aluminum and air surrounding rather well, Figure 20; it fits the experimental data with $\Delta \overline{T} = 0.2\,^0\mathrm{C}$, $\tau_1 = 1.3\,\mathrm{s}$ (1), $\Delta \overline{T} = 3.0\,^0\mathrm{C}$, $\tau_1 = 32.2\,\mathrm{s}$ (2), and $\Delta \overline{T} = 12.5\,^0\mathrm{C}$, $\tau_1 = 141.8\,\mathrm{s}$ (3). However, Eq. (3.12) does not describe the Styrofoam experiment (4). Figure 20 shows an unsuccessful attempt to fit the data with parameters $\Delta \overline{T} = 20.4\,^0\mathrm{C}$, $\tau_1 = 233.3\,\mathrm{s}$, in Eq. (3.12); the fit is relatively good only at the early stages of heating. The departures are most naturally related to the fact that Newton's cooling law, used in the boundary condition in Eq. (3.12), is not justified. Newton's cooling law describes the convective heat transfer at the interface between a solid object and a flowing environment such as air or moving fluid. In fact, this flow keeps the temperature of the flowing medium at the interface constant, which is the case most closely matched in our experiments with the aluminum cooling devices and circulating air. For still air, Newton's cooling law is not expected to work as well, but the fit is still good. In contrast, poor heat transfer properties of Styrofoam lead to its gradual heating; as a result,

Newton's cooling law is not applicable, as seen from the experimental data for Styrofoam surroundings.

The data collected in Figure 20 allow us to determine the heat transfer coefficients from the fitted values of τ_1 and $\Delta\overline{T}$. We first determine $q_1 = L\sqrt{c_p\rho / G\tau_1}$ and then find k from the equation $q_1 \tan q_1 = kL/G$. For the aluminum cooling device, k=8267 W m^{-2} K^{-1}; for circulating air, k=72 Wm^{-2} K^{-1}; and for still air, k=16 Wm^{-2} K^{-1}. The data for air are in the expected range of 10–100 W m^{-2} K^{-1} [73]. Moreover, by substituting the found values of k into Eq. (3.9) and using the experimentally measured $\Delta\overline{T}$, we find that the quantity ε_{zz}^{i}=1.8 is the same for all three experiments with different media [(1) - (3)], as it should be, since ε_{zz}^{i} is the NLC material parameter (the imaginary part of the dielectric tensor component). The same value of ε_{zz}^{i} was measured independently by using the impedance analyzer SI-1260 (Schlumberger Inc.), Figure 10, which testifies that the theoretical model describes the experimental data rather well.

The stationary temperature increase $\Delta\overline{T}$ is directly influenced by the heat generation rate determined by the electric voltage U and frequency f; according to Eq. (3.9), $\Delta\overline{T} = (1+\xi)\Delta\overline{T}_k \propto f\varepsilon_{zz}^{i}U^2$. The dependence $\Delta\overline{T} \propto U^2$ is clearly confirmed in the experiments for aluminum and air surroundings, Figure 21. Equation (3.9), matches the experimental data in Figure 21 very well when one uses the independently measured ε_{zz}^{i}=1.8 and the values of k found from the data in Figure 20 for aluminum and circulating air. Note that Figure 21 demonstrates that within the range of temperature

increases studied in this work, the possible temperature dependencies of the material parameters such as ε_{zz}^{i} and k do not change the predicted linear dependence $\Delta\overline{T} \propto U^2$.

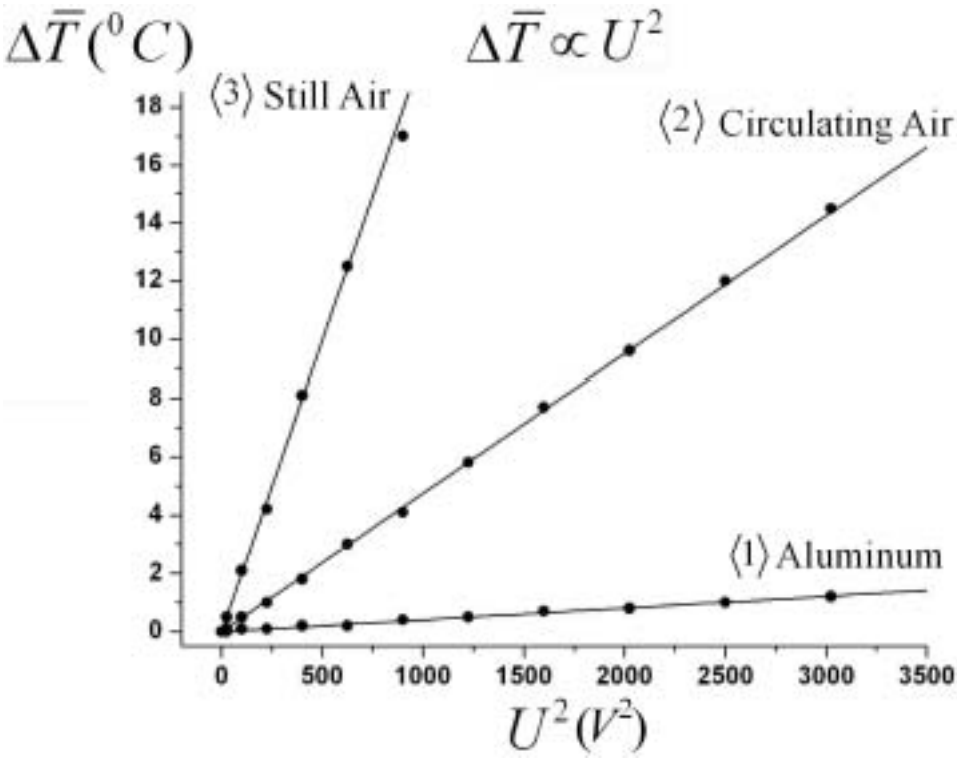

Figure 21. Voltage dependence of the stationary temperature increase $\Delta\overline{T}$ for aluminum and air surroundings, measured at a constant f =500 kHz. The initial temperature T_0=23 ^{0}C. The solid lines correspond to Eq. (3.9) with independently determined $\varepsilon_{zz}^{i} = \varepsilon_{\perp}^{i} = 1.8$ and k=8267 Wm^{-2} K^{-1} (1), k =72 Wm^{-2} K^{-1} (2), and k=16 Wm^{-2} K^{-1} (3). The accuracy of the temperature measurement is ±0.1 °C, with the error bars less than the size of the data points.

Equations (3.12) and (3.13) indicate that for a given NLC cell in a given surrounding medium the time τ_1 associated with the transition to the stationary state $\Delta\overline{T}$ does not depend on the amplitude and frequency of the applied voltage (despite the fact that $\Delta\overline{T}$ itself does depend on both of them). Figure 22 demonstrates that the dynamics of the temperature increase for the same system driven in different regimes with different voltages and frequencies can indeed be described with a single parameter τ_1. Interestingly, Figure 22(a) shows also that the driving voltage of 45 V at f =0.8 MHz produces a stronger dielectric heating effect than a higher voltage of 50 V at f =0.5 MHz. The effect is related to the fact that the frequency of 0.8 MHz is closer to the frequency $f \approx 2$ MHz at which the imaginary part $\varepsilon_{\perp}^{i}$ for the studied DFN reaches a maximum.

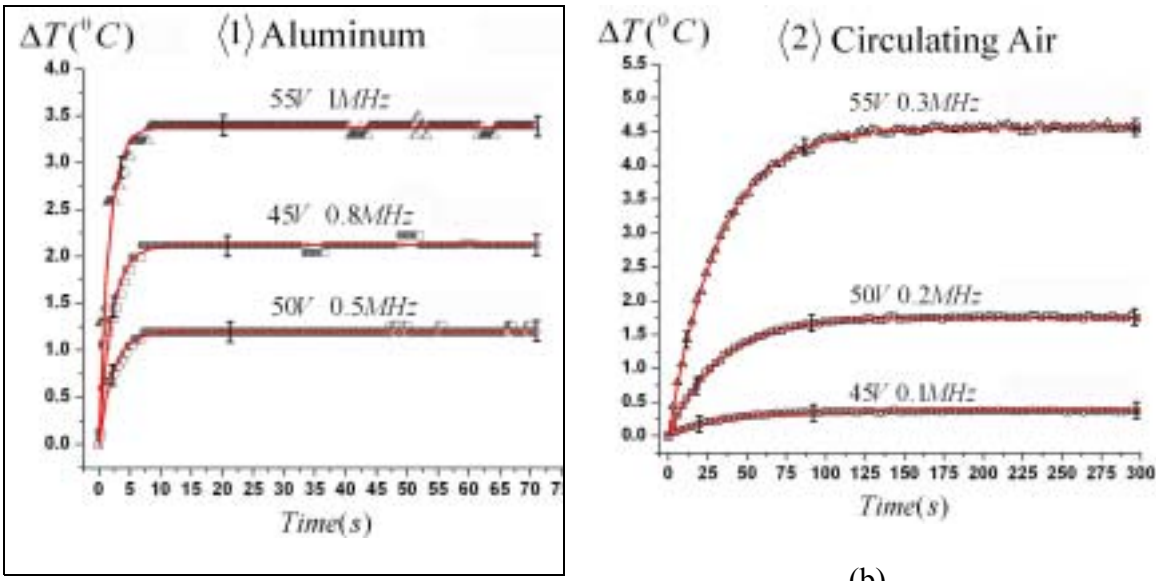

(a) (b)

Figure 22. Temperature changes of the MLC2048 cells surrounded by the aluminum cooling device (a) and by circulating air (b), caused by different electric fields. The solid

lines correspond to Eq. (3.12) with $\tau_1 = 1.5 \pm 0.2\,\mathrm{s}$ (a) and $\tau_1 = 32.2 \pm 0.3\,\mathrm{s}$ (b); $\Delta\bar{T}$ is determined experimentally. The accuracy of the temperature measurement is ±0.1 °C, and the corresponding error bars are demonstrated.

The model above indicates that the dielectric heating effect is strongly frequency dependent. There are different ways the frequency influences the temperature changes. The first mechanism is through the direct dependency $\Delta\bar{T} \propto f$, see Eq. (3.9), which is predominant when the director is not experiencing reorientation in the field and when the frequency is far from the regions of dielectric relaxation. Furthermore, $\Delta\bar{T} \propto \varepsilon_{zz}^{i}$ and the temperature changes can be caused by the frequency dependencies of the LC dielectric properties, which give rise to mechanisms 2 and 3. The real components of the LC dielectric tensor are frequency dependent and changing the frequency of the applied field can change the director orientation **n**, so that the effective imaginary dielectric permittivity $\varepsilon_{zz}^{i} = \varepsilon_{\parallel}^{i}\cos^2\theta + \varepsilon_{zz}^{i}\sin^2\theta$ changes; we will refer to this effect as mechanism 2. Finally, the most interesting thing is that the temperature changes might reflect the nonmonotonous frequency dependencies of the imaginary parts $\varepsilon_{\parallel}^{i}$ and $\varepsilon_{\perp}^{i}$ of the parallel and perpendicular components of the dielectric tensor, i.e., through distinct mechanism 3.

The three mechanisms outlined above suggest that the total frequency dependency of the temperature increase, $\Delta\bar{T} \propto f\,\varepsilon_{zz}^{i}(f)$, might be nonmonotonous, as $\varepsilon_{zz}^{i}(f)$ might be a decreasing function of *f* when *f* increases above the frequencies of the characteristic maxima for $\varepsilon_{\parallel}^{i}$ and $\varepsilon_{\perp}^{i}$.

To verify experimentally the theoretical predictions, we used the still air surrounding (the temperature changes in circulating air and with aluminum cooling devices were too insignificant) for the LC cells. The temperature changes $\Delta\bar{T}$ at each frequency and voltage were determined as the stationary values, Figure 23.

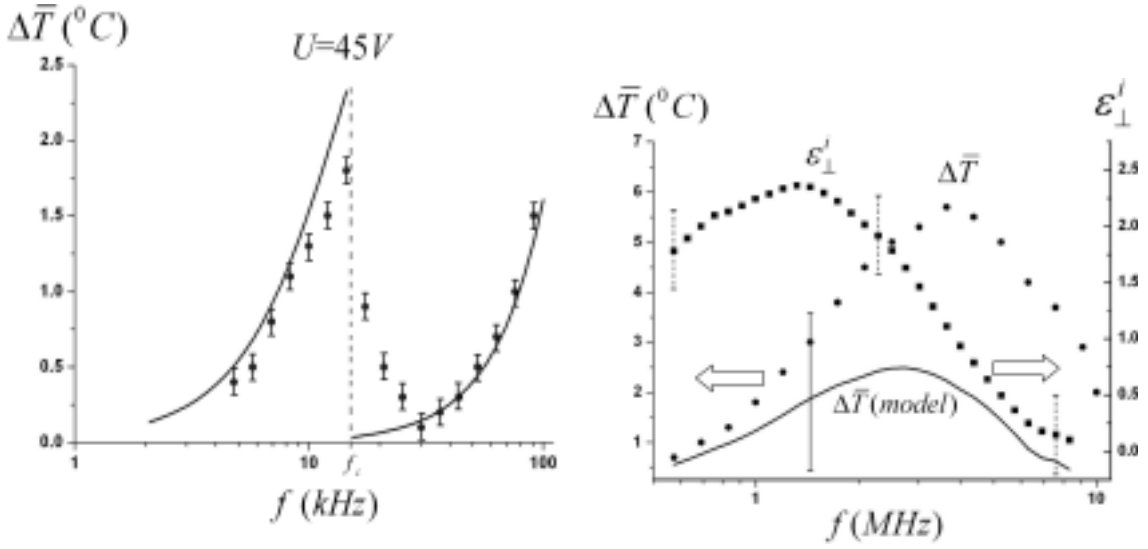

(a) (b)

Figure 23. (a) The stationary values of the temperature change $\Delta\bar{T}$ of the planar MLC2048 cell surrounded by medium (3) (still air) vs the applied frequency *f*, when *f* is in the range of the relaxation of $\varepsilon_{\parallel}^{i}$, 1–100 kHz. The solid line is the theoretical result calculated using Eq. (3.9) with most of the parameters measured directly (*f*, *U*, *L*, *d*, $\varepsilon_{\parallel}^{i}$ and $\varepsilon_{\perp}^{i}$); one parameter (*G*) was taken from Ref. [68] and one (*k*) was determined from the data shown in Figure 20. The accuracy of the temperature measurement is ±0.1 °C, and the corresponding error bars are demonstrated. (b) Frequency dependence of the stationary values of the temperature change $\Delta\bar{T}$ of the planar MLC2048 cell surrounded by medium (3) (still air) and imaginary permittivity component $\varepsilon_{\perp}^{i}$ in the high-frequency

range of 0.5–10 MHz. The solid line is calculated from Eq. (3.9) with no fitting parameters: the values of directly (f, U, L, d, $\varepsilon_{\perp}^{i}$) were measured directly; G was taken from Ref. [68] and k was determined from the data shown in Figure 20. The dashed error bar corresponds to the estimated error range of the measured $\varepsilon_{\perp}^{i}$, and the solid error bar corresponds to the estimated error range of the calculated $\Delta\overline{T}$ from the model.

Figure 23 illustrates the three mechanisms above. Figure 23(a) shows the interplay of mechanisms 1 and 2. The cell with the original planar director orientation was driven by a high voltage of 45 V at different frequencies. At low frequencies, $f < f_c$, the director deviates from the initial planar orientation with $\theta = \pi/2$. As f increases, so does the temperature change $\Delta\overline{T}$, in accordance with mechanism 1, $\Delta\overline{T} \propto f$.

However, the positive slope of $\Delta\overline{T} \propto f$ changes to a negative one near $f \approx f_c$. This reverse in the slope in Figure 23(a) can be associated with mechanism 2, i.e., with the director reorientation from the "vertical" state at low frequencies where $\Delta\varepsilon > 0$ to the "horizontal" (planar) state at $f > f_c$, where $\Delta\varepsilon < 0$, Figure 10. Such a reorientation mitigates dielectric heating near $f \approx f_c$, as in this region, $\varepsilon_{\perp}^{i} < \varepsilon_{\parallel}^{i}$. Thus the dependency $\Delta\overline{T}(f)$ in Figure 23(a) results from the combination of mechanisms 1 and 2; note that this effect of the two competing mechanisms, 1 and 2, has been already observed and explained by Schadt [19, 46].

Figure 23(b) illustrates what might be a new type of $\Delta\overline{T}(f)$ dependence that is caused by the balance of mechanisms 1 and 3. By using the same planar cell as in the

case shown in Figure 23(a), we measured the temperature increase in the high-frequency regime above 0.5 MHz, Figure 23(b). The applied voltage was small (5 V). The stability of the texture and the absence of director reorientation were verified under the microscope. We found that $\Delta\bar{T}(f)$ is nonmonotonous with a local maximum near f =4 MHz. The most plausible reason of this nonmonotonous behavior appears to be the dielectric relaxation of $\varepsilon_{\perp}(f)$ manifested by a maximum of $\varepsilon_{\perp}^{i}$ at 1.8 MHz (mechanism 3), shown in Figure 10(b). The fact that the maximum of $\Delta\bar{T}(f)$ is located at a higher f than the maximum of $\varepsilon_{\perp}^{i}$ corresponds to the contribution of mechanism 1 to the total value of $\Delta\bar{T}(f)$. Figure 23(b) shows that the nonmonotonous behavior of $\Delta\bar{T}(f)$ is qualitatively reproduced by the model curve calculated using Eq. (3.9) with no fitting parameters. The quantitative difference between the experiment and theoretical prediction of Eq. (3.9) can be attributed to the following two reasons. First, the measurements of dielectric properties using the impedance/gain phase analyzer SI-1260 are not reliable at f >1 MHz. Second, at the megahertz frequencies, the voltage acting at the liquid crystal layer is reduced as compared to the voltage applied to the entire cell by about 20%. However, this second factor should not cause the nonmonotonous behavior of $\Delta\bar{T}(f)$ by itself, as the quantity that matters is the product fU^2 that increases with f. Further experiments are needed to verify mechanism 3 quantitatively by accurately measuring the frequency dependence of $\varepsilon_{\perp}^{i}$.

To conclude this chapter, we performed a systematic theoretical and experimental study of the electric heating effects in the nematic liquid crystals in an external ac electric

field. A multilayer heat conduction model has been developed to understand how the temperature of a nematic cell confined between two plates and placed in a surrounding medium with certain thermal conductivity properties changes because of the electric heating effect. We derive the expressions describing the dynamics of temperature changes and the value of the stationary temperature increase. The temperature dynamics towards the stationary value follows the exponential law with the characteristic time τ_1 that depends on the bounding plates (their thickness L, heat capacity c_p, and thermal conductivity G) and on the heat transfer coefficient k of the surrounding medium. The stationary value of the temperature increase is a strong function of the applied voltage and nematic layer thickness, $\Delta\bar{T} \propto U^2/d$, the properties of the surrounding plates and medium, $\Delta\bar{T} \propto (1/k + L/G)$, and the field frequency, dielectric and conductive properties of the liquid crystal itself, $\Delta\bar{T} \propto f\varepsilon_0\varepsilon_{zz}^i + \sigma_{zz}/2\pi$. The conductivity contribution in our experiments becomes negligibly small at f>1 kHz. Note that some of the parameters above, such as ε_{zz}^i, are itself temperature dependent. These dependencies do not change Eq. (3.9) for the stationary values of the temperature increase, but can somewhat modify Eq. (3.6) for the temperature dynamics. In most cases, however, these corrections are small, as demonstrated by the fact that the experimental dynamics is well described by Eq. (3.6).

Our model assumes that the heat flux at the bounding plate-surrounding medium interface obeys Newton's cooling law, which is a good approximation for all practical media with a normal heat transfer; as shown in the experiment, the assumption might be

violated only in media with an extremely poor heat transfer such as Styrofoam. In the experimental part, we directly measured the temperature variations of the nematic material by a tiny thermocouple. We used the dual frequency nematic material as it allowed us to test the regions of the dielectric relaxation which are located at relatively low frequencies (tens of kilohertz). At the very same time, the frequency region of a few kilohertz and above corresponds to the situation when the electric heating caused by ionic currents is much smaller than the heating caused by dielectric relaxation. We used different surrounding media, from extremely good heat conductors such as aluminum cooling device to extremely poor conductor, Styrofoam; these two provide two limiting cases as compared to typical conditions of nematic cell exploitation in a laboratory or in commercial devices. The experiments with the good heat conductors confirmed that the NLC temperature changes are smaller in the media with a larger heat transfer coefficient *k*. The experiments confirm the theoretical predictions, namely, $\Delta\bar{T} \propto U^2/d$, $\Delta\bar{T} \propto (1/k + L/G)$, and $\Delta\bar{T} \propto f\varepsilon_0\varepsilon_{zz}^i$. The latter dependence is controlled by three different mechanisms and might be nonmonotonous. The nonmonotonous character of $\Delta\bar{T} \propto f\varepsilon_0\varepsilon_{zz}^i$ is associated with the director reorientation and with the existence of maxima in the frequency dependence of the imaginary parts of the dielectric permittivity $\varepsilon_{\parallel}^i$ and $\varepsilon_{\perp}^i$.

3.3 Conclusions

To conclude this chapter, we performed a systematic theoretical and experimental study of the electric heating effects in the nematic liquid crystals in an external ac electric field. A multilayer heat conduction model has been developed to understand how the temperature of a nematic cell confined between two plates and placed in a surrounding medium with certain thermal conductivity properties changes because of the electric heating effect. We derive the expressions describing the dynamics of temperature changes and the value of the stationary temperature increase. The temperature dynamics towards the stationary value follows the exponential law with the characteristic time τ_1 that depends on the bounding plates (their thickness L, heat capacity c_p, and thermal conductivity G) and on the heat transfer coefficient k of the surrounding medium. The stationary value of the temperature increase is a strong function of the applied voltage and nematic layer thickness, $\Delta\bar{T} \propto U^2 / d$, the properties of the surrounding plates and medium, $\Delta\bar{T} \propto (1/k + L/G)$, and the field frequency, dielectric and conductive properties of the liquid crystal itself, $\Delta\bar{T} \propto f\varepsilon_0\varepsilon_{zz}^i + \sigma_{zz}/2\pi$. The conductivity contribution in our experiments becomes negligibly small at f >1 kHz. Note that some of the parameters above, such as ε_{zz}^i, are itself temperature dependent. These dependencies do not change Eq. (3.9) for the stationary values of the temperature increase, but can somewhat modify Eq. (3.6) for the temperature dynamics. In most cases, however, these

corrections are small, as demonstrated by the fact that the experimental dynamics is well described by Eq. (3.6).

Our model assumes that the heat flux at the bounding plate-surrounding medium interface obeys Newton's cooling law, which is a good approximation for all practical media with a normal heat transfer; as shown in the experiment, the assumption might be violated only in media with an extremely poor heat transfer such as Styrofoam. In the experimental part, we directly measured the temperature variations of the nematic material by a tiny thermocouple. We used the dual frequency nematic material as it allowed us to test the regions of the dielectric relaxation which are located at relatively low frequencies (tens of kilohertz). At the very same time, the frequency region of a few kilohertz and above corresponds to the situation when the electric heating caused by ionic currents is much smaller than the heating caused by dielectric relaxation. We used different surrounding media, from extremely good heat conductors such as aluminum cooling device to extremely poor conductor, Styrofoam; these two provide two limiting cases as compared to typical conditions of nematic cell exploitation in a laboratory or in commercial devices. The experiments with the good heat conductors confirmed that the NLC temperature changes are smaller in the media with a larger heat transfer coefficient *k*. The experiments confirm the theoretical predictions, namely, $\Delta\bar{T} \propto U^2 / d$, $\Delta\bar{T} \propto (1/k + L/G)$, and $\Delta\bar{T} \propto f\varepsilon_0\varepsilon_{zz}^i$. The latter dependence is controlled by three different mechanisms and might be nonmonotonous. The nonmonotonous character of

$\Delta\bar{T} \propto f\varepsilon_0\varepsilon_{zz}^i$ is associated with the director reorientation and with the existence of maxima in the frequency dependence of the imaginary parts of the dielectric permittivity $\varepsilon_{\parallel}^i$ and $\varepsilon_{\perp}^i$.

Chapter 4

Thermodielectric Bistability

In this chapter, we report on a thermodielectric bistability in DFNs caused by the anisotropic nature of dielectric heating and director reorientation in an electric field. The bistability is a result of the positive feedback loop: director reorientation → anisotropic dielectric heating → dielectric anisotropy → director reorientation. We demonstrate both experimentally and theoretically that two states with different temperature and director orientation, namely, a cold planar (CP) state and a hot homeotropic (HH) state coexist in a LC cell for a certain frequency and amplitude range of the applied voltage.

4.1 Formulation of the problem

The phenomenon that two stable states of a system coexist under the same external conditions is known as bistability. Bistability is found in atomic systems [74], gases [75], semiconductors [76], liquid crystals [77-82], biological cells [83], etc. Bistabilities in LCs are of especially widespread interest due to their successful application in LC displays [80, 81], spatial light modulators [82], and optical information storage [77], etc. The bistabilities in LCs are caused by a balance of two different agents, such as an

electric field **E** that orients the LC director **n** in the bulk, and surface anchoring that keeps the director aligned at the bounding substrates. In this chapter, we demonstrate a novel effect, in which the bistability originates from the electric field alone, through the balance of two different mechanisms of coupling between **E** and LC, namely, director reorientation and *anisotropic* dielectric heating.

From Chapter 1 and 2, we know the direction of the director reorientation is determined by the sign of $\Delta\varepsilon$. For DFNs under the low frequency field $f < f_c$, we have positive dielectric anisotropy, $\Delta\varepsilon > 0$, and **n** reorients parallel to **E**, i.e., $\mathbf{n} \| \mathbf{E}$. If $f > f_c$, $\Delta\varepsilon < 0$, then $\mathbf{n} \perp \mathbf{E}$. The crossover frequency f_c corresponds to the dispersion region of $\varepsilon_{\|}$, and f_c is a strong monotonically increasing function of temperature. From Chapter 3, we know that the heating for DFN is essentially an *anisotropic effect*: the temperature increase is maximum when $\mathbf{n} \| \mathbf{E}$ and minimum when $\mathbf{n} \perp \mathbf{E}$, Figure 23.

The two mechanisms of coupling between **n** and DFN thus set up a possibility of a bistability of two states that can coexist at a given **E**: a cold planar (CP) state and a hot homeotropic (HH) state. The idea can be explained by the following gedanke experiment.

One starts an experiment with a DFN sandwiched between two flat electrodes. A modest electric voltage *U* is applied at $f > f_c$ (so that $\Delta\varepsilon < 0$) to stabilize the CP state, $\mathbf{n} \perp \mathbf{E}$. An increase *U* would increase the LC temperature T, up to the point T_c where the inversion frequency $f_c(T)$ exceeds f and $\Delta\varepsilon$ become positive. With $\Delta\varepsilon > 0$, the director reorients to the HH state with $\mathbf{n} \| \mathbf{E}$. The voltage $U_{CP \to HH}$ of CP $\to$ HH transition is relatively high because in the CP state the dielectric heating is minimum. In the HH

state, however, the dielectric heating is more efficient than in the CP state. The threshold $U_{HH\to CP}$ of the reverse HH$\to$CP transition, caused by decreasing U to reach T_c from above in the HH state, should be lower than $U_{CP\to HH}$. Therefore, because of the anisotropic nature of both dielectric heating and dielectric reorientation of the director, one would expect a bistability, i.e., a coexistence of the CP and HH states in the certain range of voltages, $U_{HH\to CP} < U < U_{CP\to HH}$. Below, we first demonstrate the phenomenon experimentally and then describe it with a quantitative model that, in addition to the consideration of the bulk dielectric reorientation and heating, takes into account the surface anchoring effects at the bounding plates, which hinders the occurrence of bistability rather than causes it, as in other know cases [77-82].

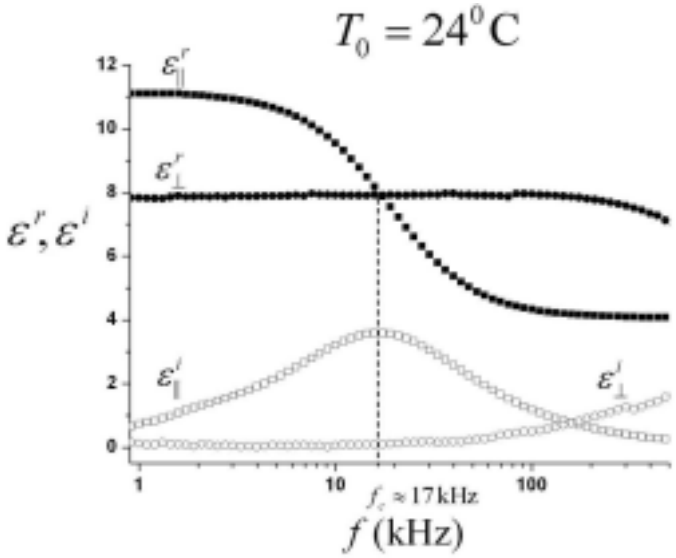

Figure 24. The measured the real (ε^r) and imaginary (ε^i) parts of the dielectric permittivity tensor of MLC2048 in the frequency range 1 kHz to 500 kHz at 24 ^{0}C. The error bars are smaller than the size of the data points.

4.2 Experiment

We used MLC2048 to demonstrate thermodielectric bistability. The real ($\varepsilon_{\|}^{r}$, $\varepsilon_{\perp}^{r}$) and imaginary ($\varepsilon_{\|}^{i}$, $\varepsilon_{\perp}^{i}$) components of the dielectric permittivity tensor of MLC2048 were measured using the Impedance/Gain-Phase analyzer SI-1260 (Schlumberger Inc.) in the range $f = (1-500)$ kHz at T_0=24.0 ^{0}C, Figure 24. The sign reversal of $\Delta\varepsilon$ is caused by the dispersion of $\varepsilon_{\|}$ and the maximum value of $\varepsilon_{\|}^{i}$ is reached at f_c.

We filled MLC2048 into a cell of a thickness d=11 μm. The indium tin oxide electrodes at the inner surfaces of the cell's bounding glass plates were coated with a polyimide layer SE-7511 (Nissan Chemicals) to set **n** perpendicular to the bounding plate; this homeotropic alignment allows us to identify the unambiguously the HH state as a "black" state in observations with crossed polarizers. The cell was placed inside a LTS-350 hotstage (Linkam) permitting temperature stabilization at 24.00 ± 0.01 ^{0}C. To improve the uniformity of thermal environment around the cell, we created an air gap between the cell and the hot stage, by separating them with two wood rods of 0.5 mm diameter. We measured the temperature T_g at the outer surface of the glass plate bounding the LC, by an attached thermocouple. According to Chapter 3, (a) the heat flux Q_{out} at the interface between the cell and the surrounding medium obeys the Newton's cooling law, i.e., $Q_{out} = k(T_g - T_0)$, where and k is the heat transfer coefficient of the cell/air interface (b) the temperature gradient across the LC layer is small, less than

0.01 ^{0}C. Thus the relation between the LC average temperature T and the measured temperature of the cell's external surface T_g at the thermal equilibrium is [84],

$$T - T_0 = (1 + Bi)(T_g - T_0), \qquad (4.1)$$

where $Bi = kL/G$ is Biot number, L=1.1 mm and G = 1 W m^{-1} K^{-1} are the thickness and thermal conductivity [68] of the glass plate, respectively. With the typical $k = 10 - 50$ W m^{-2} K^{-1} [85], Bi is very small, 0.01 to 0.05, and thus, according to (4.1), T_g yields a good quantitative measure of T.

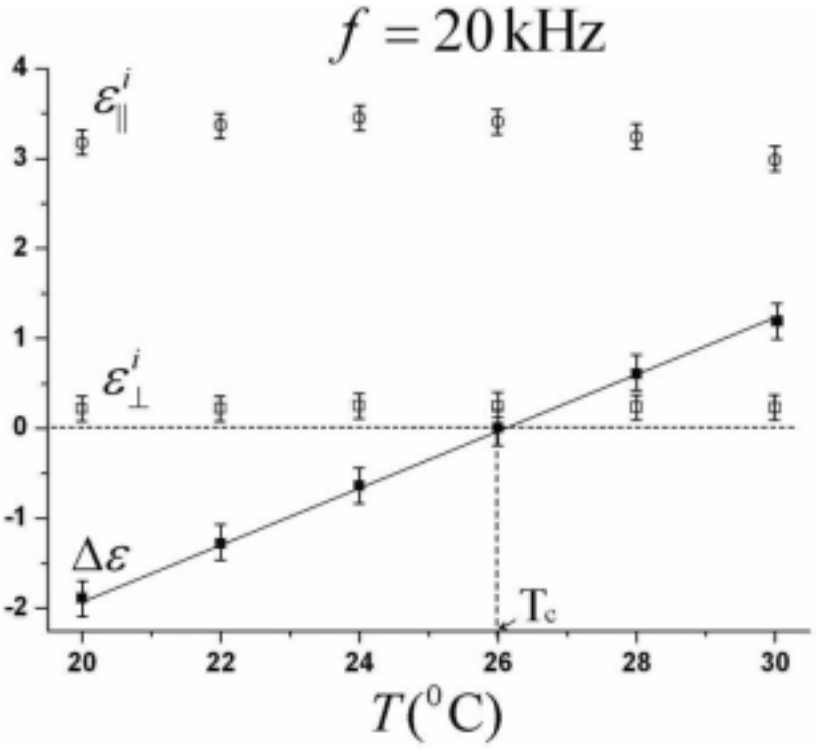

Figure 25. The imaginary dielectric permittivities ($\varepsilon_{\parallel}^{i}(T)$, $\varepsilon_{\perp}^{i}(T)$) and dielectric anisotropy ($\Delta\varepsilon(T)$) of MLC2048 at 20 kHz are plotted as a function of temperature. The straight line corresponds to the linear fit for $\Delta\varepsilon(T)$, Eq.(4.4).

We applied harmonic voltage $\tilde{U} = \sqrt{2}U \cos 2\pi ft$ with varying RMS voltage U. We have chosen $f = 20\,\text{kHz}$, because T_c for this frequency is 26 ^{0}C, i.e., slightly larger than T_0, Figure 25. The RMS voltage was changed in steps of 0.2 V with 400 s equilibrium time; the latter is enough to achieve the equilibrium temperature within 0.01 ^{0}C from Chapter 3, the accuracy of the temperature control. The state of the cell placed between two crossed polarizers of a microscope was monitored through the textural (Figure 26) and light transmittance changes (Figure 27); the polarizers were aligned to maximize the transmittance in the CP state.

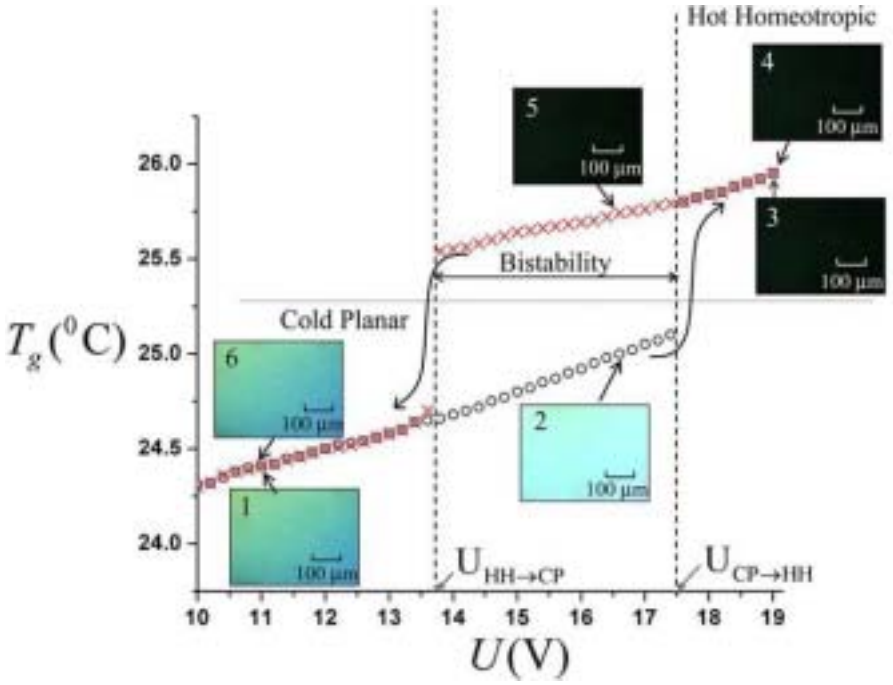

Figure 26. The thermoelectric bistability: the measured temperature T_g vs increasing (circles) and decreasing (crosses) applied voltage. The inserts exhibits images in a polarizing microscope with crossed polarizers.

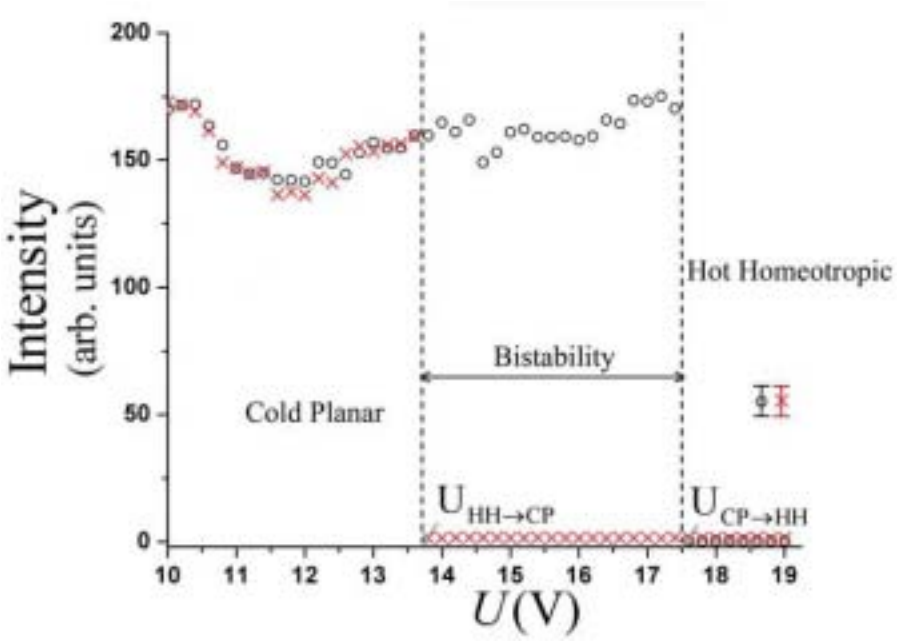

Figure 27. The transmitted light intensity vs increasing (circles) and decreasing (crosses) applied voltage. The error bars correspond to the intensity data in CP state; in HH state the error bars are smaller than the cross size.

The initial homeotropic state transforms into a state with **n** tilted away from **E** when the applied voltage exceeds the Frederiks threshold $U_F^0 = \pi(K_{33}/\varepsilon_0|\Delta\varepsilon(T_0)|)^{1/2} \approx 6\,\mathrm{V}$; this state is an analog of the CP state in the gedanke experiment, the only difference is that **n** is not strictly parallel to the bounding plates (because of the surface anchoring at the bounding plates); we will continue label this "cold tilted" state as the CP state. The CP state appears as a bright texture under the crossed polarizers (inserts 1 and 2 in Figure 26); the light transmission is high, Figure 27. Small increments of voltage lead to small increments of the measured cell temperature T_g. However, at some voltage $U_{CP\to HH}$, the CP structure transforms abruptly into a dark HH texture (insert 3 in Figure 26 and Figure

27) with a substantial increase of T_g. Further voltage increase produces relatively small temperature increases, Figure 26. In the reverse process of lowering the voltage, the HH state persists until the voltage is reduced to $U_{HH\to CP}$, well below $U_{CP\to HH}$ (by 3.8 V, Figure 26 and Figure 27). The cell becomes transparent again, as the director tilts away from the homeotropic orientation, insert 6 in Figure 26. The experiment clearly shows that the bistability regime in the range $U_{HH\to CP} < U < U_{CP\to HH}$.

4.3 Model

The model of the phenomenon is based on the self-consistent consideration of the temperature and director fields in a cell with strong surface anchoring. The harmonic voltage $\tilde{U} = \sqrt{2}U\cos 2\pi ft$ creates an electric field $\mathbf{E} = U\hat{\mathbf{z}}/d$ that is assumed to be homogeneous within the LC as $\Delta\varepsilon$ is small for the frequency range of interest.

From Chapter 3, we know the thermal balance between the heat generation and dissipation $Q_{in} = Pd/2 = Q_{out}$, determines the equilibrium cell temperature T:

$$T = T_0 + \frac{\pi(1+Bi)\, f\, \varepsilon_0 \varepsilon_{zz}^i U^2}{kd}. \qquad (4.2)$$

The characteristic time of the temperature dynamics is $\tau_T = c_p \rho L^2 / G q_1^2$, where c_p is the heat capacity of the glass plate, ρ is the glass density, and $q_1 \approx Bi^{1/2}$ is the smallest positive root of the equation $q_1 \tan q_1 = Bi$. The values of τ_T has been discussed in (3.13), with the magnitude range from [1, 100] s depending on the surrounding medium. Therefore τ_T is much larger than the director reorientation time $\tau \sim 10^{-2}$ s, the director

configuration can be found as an equilibrium state of a cell with elastic and dielectric properties that correspond to the current temperature.

Let us start with situation when the director orientation at the bounding plates is not fixed by surface anchoring, to show the essence of the effect and the importance of dielectric heating anisotropy. In the anchoring-free case, the equilibrium state is either strictly homeotropic, $\mathbf{n} \parallel \mathbf{E}$, when $\Delta\varepsilon(T) > 0$, or strictly planar $\mathbf{n} \perp \mathbf{E}$, when $\Delta\varepsilon(T) < 0$. Thus, both transitions should start at $T = T_c$ and the bistability range $U_{HH\to CP} < U < U_{CP\to HH}$ should be determined by anisotropy of the dielectric heating, as $U_{HH\to CP} = U_0 / (\varepsilon_{\parallel}^i)^{1/2}$ and $U_{CP\to HH} = U_0 / (\varepsilon_{\perp}^i)^{1/2}$, where $U_0 = [(T_c - T_0)kd / (\pi(1 + Bi) f \varepsilon_0)]^{1/2}$. Note that the anisotropy of dielectric heating must be positive, i.e. $\varepsilon_{\parallel}^i > \varepsilon_{\perp}^i$, for the effect to take place.

In a cell with **n** fixed by surface anchoring, the equilibrium director configuration has a well-known analytical solution [86]. For small $\Delta\varepsilon < 0$, and for one constant approximation of LC elasticity, this solution relates to ε_{zz}^i, U and the maximum angle θ_m in the middle of the LC layer:

$$U = 2\left(\frac{K}{\varepsilon_0 |\Delta\varepsilon(T)|}\right)^{1/2} \mathbf{K}(\sin^2\theta_m), \quad \varepsilon_{zz}^i = \varepsilon_{\perp}^i + (\varepsilon_{\parallel}^i - \varepsilon_{\perp}^i)\frac{\mathbf{L}(\sin^2\theta_m)}{\mathbf{K}(\sin^2\theta_m)}, \qquad (4.3)$$

where K is the elastic constant of the LC, $\mathbf{K}(\sin^2\theta_m)$ and $\mathbf{L}(\sin^2\theta_m)$ are the complete elliptic integrals of the first and second kind, respectively [87].

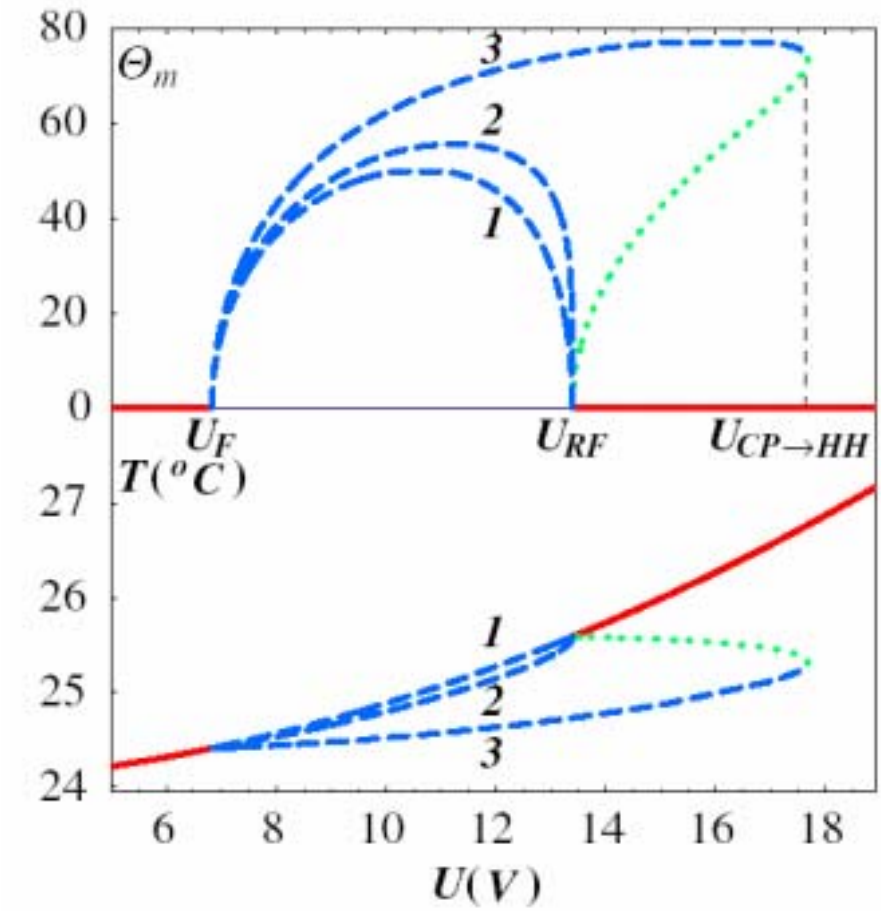

Figure 28. The simulation of thermodielectric bistability exhibited in $\theta_m(U)$ and $T(U)$ for CP (dashed curves), HH (solid curves) and unstable (dotted curves) states in a homeotropic cell with different $\varepsilon_\perp^i$: (1) 0.45, (2) 2.57, (3) 3.2. The other parameters correspond to MLC2048 and the experiment presented above. The heat transfer coefficient of the air/glass interface k=20 W m^{-2} K^{-1} is chosen to make curve 3 close to the experimental data.

To describe the bistability, in addition to Eqs (4.2) and (4.3), one needs to specify the dependence of $\Delta\varepsilon(T)$; Figure 25 shows that it follows a linear behavior,

$$\Delta\varepsilon(T) = a(T_c - T), \qquad (4.4)$$

where $a = 0.316\ ^0\text{C}^{-1}$, $T_c = 26\ ^0\text{C}$.

Eqs. (4.2)-(4.4) allow us to find an analytical solution describing $T(U)$ and $\theta_m(U)$, Figure 28. The bistability is controlled by the anisotropy of dielectric heating, $\Delta\varepsilon^i = \varepsilon_{\|}^i - \varepsilon_{\perp}^i$. In Figure 28, we fix $\varepsilon_{\|}^i = 3.5$ (which is characteristic of MLC2048) and analyze the scenarios for three different $\varepsilon_{\perp}^i$'s, corresponding to $\Delta\varepsilon^i = 0$ (curve 1), $\Delta\varepsilon^i = 0.93$ (curve 2), $\Delta\varepsilon^i = 3.1$ (curve 3). Curve 1 describes the "usual" monostable sequence characteristic of zero heating anisotropy. The LC layer, originally in the homeotropic state, experiences a regular Frederiks transition into a tilted CP state above some modest threshold U_F, , , curve 1. Further voltage increase leads to an increase of θ_m but it also increases T. Because of the latter, $\Delta\varepsilon$ decreases to zero and at some U_{RF}, the cell experiences a reverse Frederiks transition, back to $\theta_m = 0$. Decreasing U would result in the reverse sequence of transitions without any hysteresis. The scenario changes completely if the heating anisotropy is positive and large enough, curve 3. The original state $\theta_m = 0$ is converted into the CP state $\theta_m > 0$ at the same U_F, but because the heat production in this state is relatively slow $\varepsilon_{\perp}^i << \varepsilon_{\|}^i$, the dielectric anisotropy $\Delta\varepsilon$ remains positive and the CP state is retained even for voltages above U_{RF}; it transforms abruptly into the HH state returns into the CP state only at some $U_{HH\to CP} > U_{RF}$. Upon reduction of voltage, the HH state returns into the CP state at $U_{HH\to CP} = U_{RF}$, hence a bistability. Finally, curve 2 is a critical regime separating the monostable and bistable behaviors.

The model (curve 3) describes the experimental data very closely, as evident from the predicted voltage and temperature range of the bistability, compare Figure 26 and Figure 28. Clearly, some model simplifications, such as one-constant elasticity, exact value of k, and cell imperfections, such as director distortions around the spacers or finite electric conductivity of the cell, might cause quantitative discrepancies, but the overall agreement is good.

4.4 Conclusions

To conclude this chapter, we observed and interpreted the thermodielectric bistability that is caused by a competition of dielectric heating and director reorientation of the LC in an electric field. For the effect to occur, the dielectric heating should be anisotropic (i.e., dependent on the director orientation with respect to the applied electric field), a feature that has not been appreciated much in the literature so far. The thermodielectric bistability might be of practical importance, because (a) the optical contrast between the HH and CP states is extremely sharp, as the director reorients substantially, from $\theta_m \approx 0^0$ to $\theta_m \approx 70^0$ at the HH-CP transition, Figure 28; (b) the states can be switched between with a very low power when the frequency of the applied voltage frequency is only slightly above the crossover frequency.

Chapter 5

CONCLUSION

Orientational dynamics of NLCs in the electric field caused by dielectric anisotropy of these materials is a fundamental physical phenomenon that is at the heart of numerous modern technologies. The finite rate of dielectric relaxation in nematic liquid crystals which has been ignored previously can cause profound effects in the dielectric reorientation of the director, as demonstrated in this dissertation. The following are the main results of our research.

First, we derived an expression for the electric displacement $\mathbf{D}(t)$ as the function of not only the present value of the electric filed $\mathbf{E}(t)$, but also its past values and also the present and past configurations of the director field. By characterizing electrooptical response of dual-frequency materials, we demonstrated that our model correctly describes the effects of director reorientation when the switching time is close to the dielectric relaxation time, while the classic "instantaneous response" model predicts a behavior opposite to the one observed in the experiment.

Second, we observed and explained the bistability effect, caused by the balance of anisotropic dielectric heating and field-induced director orientation. The bistability is a result of the positive feedback loop: director reorientation $\rightarrow$ anisotropic dielectric

heating → dielectric anisotropy → director reorientation. We demonstrate both experimentally and theoretically in Chapter 4 that two states with different temperature and director orientation, namely, a cold planar (CP) state and a hot homeotropic (HH) state coexist in a LC cell for a certain frequency and amplitude range of the applied voltage.

Third, we studied electric-field-induced heating of the nematic cells, which is an issue of significant practical importance, especially for the dual-frequency materials, properties of which are strongly temperature-dependent. To describe the effect, we developed a multilayer heat conduction model and derived a formula that connects the temperature changes to the thermal properties of the medium surrounding the liquid crystal cell, electric field amplitude, and the dielectric properties of the liquid crystal.

The results of this thesis are of both fundamental and practical importance. The fundamental importance is clear as there were no models to describe how the electric field would influence the director orientation when the characteristic frequency of the field is close to (or higher than) the characteristic frequency of dielectric relaxation. From the practical point of view, the developed model can be used to optimize the switching speed of electrooptical devices based on liquid crystals. The thermodielectric bistability might find practical application as the optical contrast between the two stable states is extremely high and the states can be switched with a low electric field.

Overall, this dissertation comprehensively explored how the dielectric relaxation affects the nematic liquid crystal director dynamics. Further directions of study might be:

(1) To apply the model of dielectric memory effect to other condensed matter systems under the influence of a modulated electric field. In many cases, the dielectric relaxation time is close to the typical time of the external field modulation or structural reorientation of the system and thus a model similar to the model proposed above for the NLC, would be in order.

(2) To use the model above to optimize the shape of the driving voltage pulses so that the director reorientation is as fast as possible.

REFERENCES

1. deGennes, P.G. and J. Prost, *The Physics of Liquid Crystals*. 2 ed. 1997, New York: Oxford University Press.
2. Fréedericksz, V. and V. Zolina, Trans. Faraday Soc., 1933. **29**: p. 919.
3. Blinov, L.M. and V.G. Chigrinov, *Electrooptical Effects in Liquid Crystal Materials*. 1994, New York: Springer.
4. Kleman, M. and O.D. Lavrentovich, *Soft Matter Physics: An Introduction*. 2003, New York: Springer-Verlag.
5. Böttcher, C.J.F. and P. Bordewijk, *Theory of Electric Polarization*. Vol. 2. 1978, New York: Elsevier.
6. deJeu, W.H., *Physical properties of liquid crystalline materials*. 1980, New York: Gordon and Breach.
7. Fröhlich, H., *Theory of Dielectrics*. 2 ed. 1958, London: Oxford University Press.
8. Golovin, A.B., S.V. Shiyanovskii, and O.D. Lavrentovich, Appl. Phys. Lett., 2003. **83**: p. 3864.
9. Takanashi, H., J.E. Maclennan, and N.A. Clark, Jpn. J. Appl. Phys, 1998. **37**: p. 2587.
10. McManamon, P.F., T.A. Dorschner, and L.J. Barnes, Opt. Eng., 1993. **32**: p. 2657.
11. Dayton, D., et al., Appl. Opt., 2001. **40**: p. 2345.
12. Wu, S.T., et al., J. Appl. Phys, 2000. **77**: p. 957.

13. Wu, S.T. and C.S. Wu, J. Appl. Phys, 1989. **65**: p. 527.

14. Haase, W. and S. Wrobel, *Relaxation Phenomena*. 2003, New York: Springer.

15. Jackson, J.D., *Classical Electrodynamics*. 2 ed. 1975, New York: John Willey & Sons, Inc.

16. Hill, N., et al., *Dielectric Properties and Molecular Behavior*. 1969, London: Van Nostrand.

17. Jonscher, A.K., *Dielectric Relaxation in Solids*. 1983, London: Chelsea Dielectric Press.

18. Scaife, B.K.P., *Principle of Dielectrics*. 1998, Oxford: Clarendon Press.

19. Schadt, M., *Low-Frequency Dielectric Relaxations in Nematics and Dual-Frequency Addressing of Field Effects.* Mol. Cryst. Liq. Cryst., 1982. **89**: p. 77.

20. Debye, P., *Polar Molecules*. 1929, New York: Dover.

21. Frölich, H., *Theory of Dielectrics*. 1949, London: Oxford University Press.

22. A.Sugget, *Dielectric and Related Molecular Processes*, ed. M.Davies. Vol. 1. 1972, London: Chemical Society.

23. Böttcher, C.J.F., et al., *Theory of Electric Polarization*. Vol. 1. 1973, New York: Elsevier.

24. F.S.Tse and G.G.Raju, *Dielectrics in Electric Fields*. 2003, New York: Marcel Dekker, Inc.

25. K.S.Cole and R.H.Cole, J. Chem. Phys, 1949. **9**: p. 341.

26. Cole, K.S. and R.H. Cole, J. Chem. Phys, 1941. **9**: p. 341.

27. Cole, K.S. and R.H. Cole, J. Chem. Phys, 1942. **10**: p. 98.

28. Davidson, D.W. and R.H. Cole, J. Chem. Phys, 1950. **18**: p. 1417.

29. Davidson, D.W. and R.H. Cole, J. Chem. Phys, 1951. **19**: p. 1484.

30. Havriliak, S. and S. Negami, J. Polym. Sci. C, 1966. **14**: p. 99.

31. Maier, W. and A. Saupe, Z.Naturforsch, 1958. **A13**: p. 564.

32. Maier, W. and A. Saupe, Z. Naturforsch, 1959. **A14**: p. 882.

33. Maier, W. and A. Saupe, Z. Naturforsch, 1960. **A15**: p. 287.

34. Martin, A.J., G. Meier, and A. Saupe, Symp. Faraday Soc., 1971. **5**: p. 119.

35. Coffey, W.T., Y.P. Kalmykov, and J.T. Waldron, Liq. Cryst., 1995. **18**: p. 677.

36. Kalmykov, Y.P. and W.T. Coffey, Liq. Cryst., 1998. **25**: p. 329.

37. L.M.Blinov, *Electro-optical and magneto-optical properties of liquid crystals*. 1983, New York: Wiley.

38. Weise, H. and A. Axmann, Z. Naturforsch, 1966. **21a**: p. 1316.

39. A.B.Golovin, S.V.Shiyanovskii, and O.D.Lavrentovich, Appl. Phys. Lett, 2003. **83**: p. 3864.

40. Belyaev, B.A., et al., Physics of the Solid State, 2000. **42**: p. 577.

41. Hourri, A., et al., Liq. Cryst., 2002. **29**: p. 456.

42. Price, A.H. and D. Davies, J. Chem. Soc., Faraday Trans, 1997. **93**(9): p. 1775.

43. Bose, T.K., et al., Phys. Rev. A., 1987. **36**: p. 5767.

44. Yin, Y., et al., Mol. Cryst. Liq. Cryst., 2004. **421**: p. 133.

45. Belyaev, B.A., et al., Physics of the Solid State, 2004. **46**: p. 574.

46. Schadt, M., Mol. Cryst. Liq. Cryst., 1981. **66**: p. 319.

47. Wen, C.H. and S.T. Wu, Appl. Phys. Lett, 2005. **86**: p. 231104.

48. Haus, H.A. and J.R. Melcher, *Electromagnetic Fields and Energy*. 1989, Englewood Cliffs: Prentice Hall.

49. H.K.Bucher, R.T.Klingbiel, and J.P.VanMeter, Appl. Phys. Lett, 1974. **25**: p. 186.

50. G.M.Clark, Microelectronics Journal, 1981. **12**(3): p. 26.

51. M.Schadt, Appl. Phys. Lett, 1982. **41**: p. 697.

52. H.Fujimura, Jpn. Kokai Tokkyo Koho, 1986: p. 13.

53. R.L.Hubbard, *Twisted-nematic liquid-crystal material and dual-frequency-addressable cell therefrom*. 1988: U.S. p. 14.

54. S.Suyama, M.Date, and H.Takada, Jpn. J. Appl. Phys, 2000. **39**: p. 480.

55. Z.Lin, et al., Mol. Cryst. Liq. Cryst., 1992. **220**: p. 29.

56. T.Gotoh and H.Murai, Appl. Phys. Lett, 1992. **60**: p. 392.

57. P.Nolan and D.Coates, Mol. Cryst. Liq. Cryst., 1991. **8**: p. 75.

58. X.Ming and D.Yang, Jpn. J. Appl. Phys, 1999. **38**: p. 6827.

59. X.Ming and D.Yang, Appl. Phys. Lett, 1997. **70**: p. 720.

60. P.Debye, *Polar Molecules*. 1929, New York: Dover.

61. Cole, K.S. and R.H. Cole, J. Chem. Phys, 1949. **9**: p. 341.

62. Kreul, H.G., S. Urban, and A. Wurflinger, Phys. Rev. A., 1992. **45**: p. 8624.

63. J.Fourier, *The analytical theory of heat*. 1955, New York: Dover.

64. Hiroshi-Ono and Kazuaki-Shibata, J. Phys. D: Appl. Phys., 2000. **33**: p. L137.

65. A.V.Luikov, *Analytical Heat Diffusion Theory*. 1968, New York: Academic Press.

66. http://www.matsceng.ohio-state.edu/mse205/lectures/chapter20/chap20.pdf.

67. K.K.Chawla, *Composite Materials*. 2 ed. 2003, Norwell, MA: Krishan Kumar.

68. http://www.valleydesign.com/sodalime.htm.

69. M.Schadt, *Low-Frequency Dielectric Relaxations in Nematics and Dual-Frequency Addressing of Field Effects.* Mol. Cryst. Liq. Cryst., 1982. **89**: p. 77.

70. M.Schadt, Mol. Cryst. Liq. Cryst., 1981. **66**: p. 319.

71. B.A.Belyaev, et al., *Dielectric Properties of Liquid Crystals of the Cyano Derivative Compounds with Different Fragments in the Molecular Core.* Physics of the Solid State, 2003. **46**: p. 574.

72. T.K.Bose, et al., Phys. Rev. A., 1987. **36**: p. 5767.

73. Bejan, A., *Heat Transfer*. 1993, New York: John Wiley & Sons.

74. Hehlen, M.P., et al., Phys. Rev. Lett., 1994. **73**: p. 1103.

75. Gibbs, H.M., S.L. McCall, and T.N.C. Venkatesan, Phys. Rev. Lett., 1976. **36**: p. 1135.

76. Miller, D.A.B., S.D. Smith, and A. Johnston, Appl. Phys. Lett., 1979. **35**: p. 658.

77. Bortolozzo, U. and S. Residori, Phys. Rev. Lett., 2006. **96**: p. 037801.

78. Wen, B. and C. Rosenblatt, Phys. Rev. Lett., 2002. **89**: p. 195505.

79. Kim, J.H., M. Yoneya, and H. Yokoyama, Nature, 2002. **420**: p. 159.

80. Ramdane, O.O., et al., Phys. Rev. Lett., 2000. **84**: p. 3871.

81. Yang, D., et al., J. Appl. Phys, 1994. **76**: p. 1331.

82. Clark, N.A. and S.T. Lagerwall, Appl. Phys. Lett, 1980. **36**: p. 899.

83. Ferrell, J.E., Curr. Opin. Chem. Biol, 2002. **14**: p. 140.

84. Luikov, A.V., *Analytical Heat Diffusion Theory*. 1968, New York: Academic Press.

85. Turner, R.H. and Y.A. Cengel, *Fundamentals Of Thermal-fluid Sciences*. 2 ed. 2004, New York: McGraw-Hill.

86. Deuling, H.J., Mol. Cryst. Liq. Cryst., 1972. **19**: p. 123.

87. Abramowitz, M. and I.A. Stegun, *Handbook of Mathematical Functions*. 1970, New York: Dover.